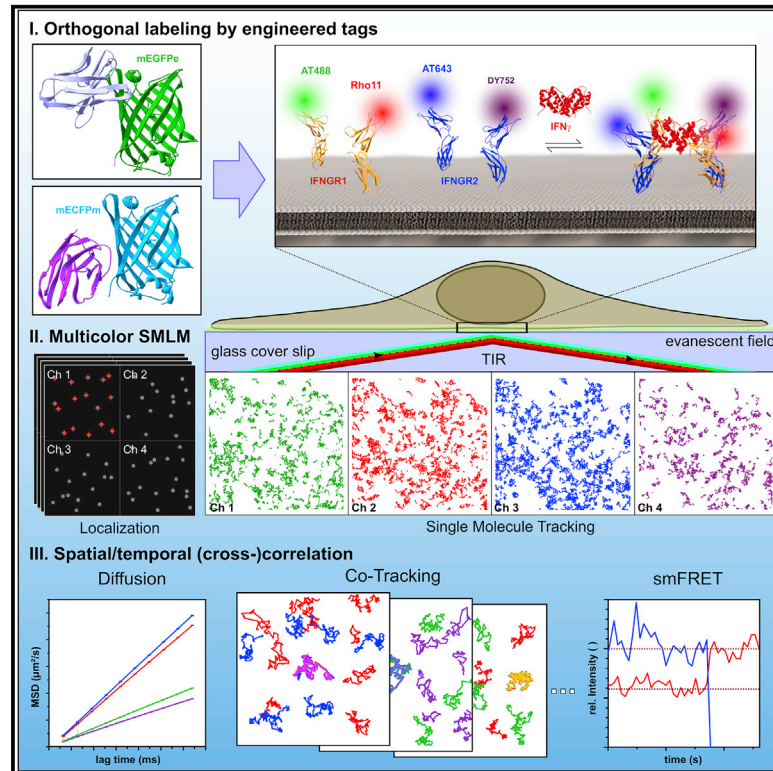**Report**

Four-color single-molecule imaging with engineered tags resolves the molecular architecture of signaling complexes in the plasma membrane

Graphical abstract

Authors

Junel Sotolongo Bellón, Oliver Birkholz, Christian P. Richter, ..., Mark R. Walter, Rainer Kurre, Jacob Piehler

Correspondence

rainer.kurre@uos.de (R.K.), piehler@uos.de (J.P.)

In brief

Sotolongo Bellón et al. describe a comprehensive workflow for analyzing diffusion and interaction of cell surface receptors by multicolor single-molecule imaging. Based on engineered orthogonal labeling in combination with spatiotemporal cross-correlation techniques and single-molecule FRET, they identify ligand-induced homo- and heterodimerization of the interferon-γ receptor in live cells.

Highlights

- Engineered nanobody targets enable selective and efficient cell surface labeling

- Single-molecule co-tracking robustly identifies ligand-induced receptor dimerization

- Single-molecule FRET reveals the geometry of signaling complexes in live cells

- Simultaneous four-color single-molecule imaging resolves homo- and heterodimerization

CellPress

Cell Reports Methods

Report

Four-color single-molecule imaging with engineered tags resolves the molecular architecture of signaling complexes in the plasma membrane

Junel Sotolongo Bellón,[1,5] Oliver Birkholz,[1,5] Christian P. Richter,[1,5] Florian Eull,[1] Hella Kenneweg,[1] Stephan Wilmes,[1,2] Ulrich Rothbauer,[3,5] Changjiang You,[1] Mark R. Walter,[4] Rainer Kurre,[1,*] and Jacob Piehler[1,6,*]

[1]Department of Biology and Center for Cellular Nanoanalytics (CellNanOs), Osnabrück University, Osnabrück, Germany
[2]Division of Cell Signalling and Immunology, University of Dundee, School of Life Sciences, Dundee, UK
[3]Pharmaceutical Biotechnology, Eberhard-Karls-University, Tübingen, Germany
[4]Department of Microbiology, University of Alabama at Birmingham, Birmingham, AL, USA
[5]NMI Natural and Medical Sciences Institute at the University of Tübingen, Reutlingen, Germany
[5]These authors contributed equally
[6]Lead contact
*Correspondence: rainer.kurre@uos.de (R.K.), piehler@uos.de (J.P.)
https://doi.org/10.1016/j.crmeth.2022.100165

MOTIVATION Unraveling the spatiotemporal organization and dynamics of receptors in the plasma membrane remains a key challenge for our mechanistic understanding of cellular signaling. Many of the current models in the field propose pre-organization at molecular and supramolecular scale. Live-cell single-molecule localization microscopy offers exciting possibilities for scrutinizing such models, but a robust methodology is still lacking. To meet this challenge, we have developed a comprehensive workflow covering high-fidelity labeling as well as dedicated multicolor single-molecule imaging and analysis techniques.

SUMMARY

Localization and tracking of individual receptors by single-molecule imaging opens unique possibilities to unravel the assembly and dynamics of signaling complexes in the plasma membrane. We present a comprehensive workflow for imaging and analyzing receptor diffusion and interaction in live cells at single molecule level with up to four colors. Two engineered, monomeric GFP variants, which are orthogonally recognized by anti-GFP nanobodies, are employed for efficient and selective labeling of target proteins in the plasma membrane with photostable fluorescence dyes. This labeling technique enables us to quantitatively resolve the stoichiometry and dynamics of the interferon-γ (IFNγ) receptor signaling complex in the plasma membrane of living cells by multicolor single-molecule imaging. Based on versatile spatial and spatiotemporal correlation analyses, we identify ligand-induced receptor homo- and heterodimerization. Multicolor single-molecule co-tracking and quantitative single-molecule Förster resonance energy transfer moreover reveals transient assembly of IFNγ receptor heterotetramers and confirms its structural architecture.

INTRODUCTION

Development, homeostasis, and protection from pathogens are essential for life of multicellular organisms and critically rely on cellular communication via transmembrane receptors. Despite detailed knowledge about components of downstream signaling pathways, qualitative and quantitative correlation of input signals and cellular decisions has so far remained highly challenging. There is increasing evidence that considerable additional complexity in signal processing is encoded in the spatiotemporal organization and dynamics of signaling molecules (Kinkhabwala and Bastiaens, 2010; Moraga et al., 2014). Intricate, hierarchical

nanoscopic compartmentalization at the plasma membrane (PM) (Bernardino de la Serna et al., 2016; Kusumi et al., 2012) has emerged as a key principle of spatiotemporal regulation of cellular signaling, but the underlying mechanisms have remained controversially debated (Garcia-Parajo et al., 2014; Grecco et al., 2011; Honigmann and Pralle, 2016). Single-molecule fluorescence microscopy (SMFM) provides a unique methodological repertoire to resolve spatial distribution, mobility, and interaction of signaling complexes with utmost spatial and temporal resolution (Asher et al., 2021; Cambi and Lidke, 2012; Kusumi et al., 2014; Stone et al., 2017; Wilmes et al., 2020; Yu, 2016). These methods are based on the ability to localize single emitters
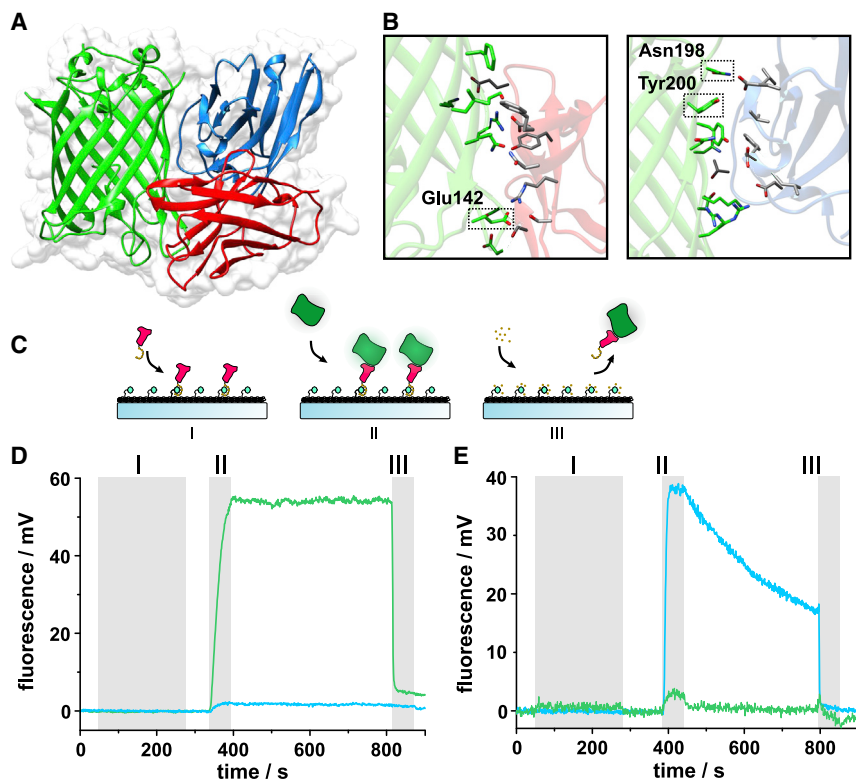
Figure 1. Engineered GFP variants for orthogonal recognition by enhancer (EN) and minimizer (MI) nanobodies

(A) Overlay of the crystal structures of the complexes of GFP (green) with EN (red) and MI (blue) (PDB: 3K1K and 3G9A, respectively) highlighting distinct epitopes, yet competitive binding.

(B) Enlarged view of the binding interfaces. Residues mutated for selectively destabilizing recognition by EN (left) and MI (right) are highlighted by dotted rectangles.

(C–E) Quantitative interaction analysis by TIRF spectroscopy in a flow-through system. (C) Schematic depiction of the stepwise nanobody immobilization onto tris-NTA functionalized surfaces loaded with Ni(II) ions (I), injection of the GFP variants (II), and regeneration of the surface by imidazole (III). (D and E) Real-time kinetics of immobilized EN (D) and MI (E) interacting with mEGFPe (green curves) and mECFPm (cyan curves). Injections corresponding to the steps shown in (C) are highlighted by gray shading.

beyond the diffraction limit with a precision down to the dimension of macromolecules (Snyder et al., 2004; Thompson et al., 2002). Interactions between proteins in the PM can be reliably detected with very high spatial and temporal resolution by single-molecule co-localization or by co-tracking complexes (Brameshuber and Schutz, 2012; da Rocha-Azevedo et al., 2020; Kasai et al., 2011; Low-Nam et al., 2011; Moller et al., 2020; Wilmes et al., 2015). However, reliable imaging and quantification of receptor interaction and dynamics in live cells by SMFM has remained challenging, as several major requirements have to be met: (1) selective and efficient labeling of target proteins in the PM with photostable fluorophores in multiple colors, (2) rapid time-lapse imaging of multiple channels with minimum photobleaching, and (3) comprehensive analysis including single molecule localization as well as spatial and spatiotemporal analysis with auto- and cross-correlation for all channels.

Here, we have developed key tools for robustly coping with this entire workflow. Single-chain antibody fragments (nanobodies, NBs) were employed as potent labeling reagents (Albrecht et al., 2015; Platonova et al., 2015; Ries et al., 2012; Virant et al., 2018). To specifically label different receptor subunits, we engineered CFP and GFP variants, which are orthogonally recognized by two different anti-GFP NBs, "enhancer" (EN) and "minimizer" (MI) (Kirchhofer et al., 2010). These NBs bind their target with very high on-rates and are therefore particularly suitable for achieving a degree of labeling (DOL) close to one with negligible non-specific background. Based on this labeling strategy, we have established live-cell four-color single-molecule imaging for quantifying receptor assembly and dynamics in the PM

of live cells. In conjunction with rigorous image analysis, these tools were successfully applied to unravel the stoichiometry of the interferon-γ (IFNγ) receptor signaling complex in the PM of live cells by multicolor single-molecule co-tracking and Förster resonance energy transfer (FRET) approaches. Our studies clearly identify ligand-induced homo- and heterodimerization of IFNγ receptor subunits, rather than preformed receptor dimers or oligomers that are currently assumed for the IFNγ receptor signaling complex (Blouin et al., 2016; Krause et al., 2002, 2006b).
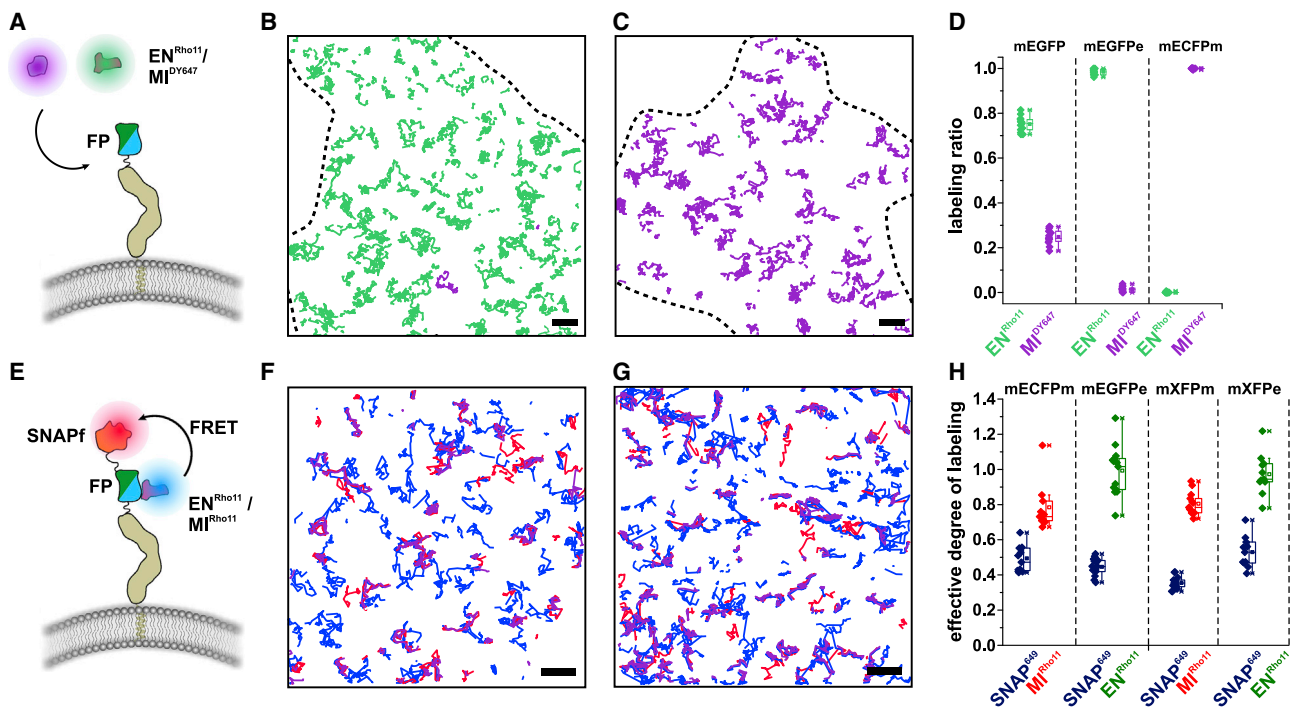
RESULTS

Engineering of mEGFP variants orthogonally recognized by nanobodies EN and MI

EN and MI competitively bind GFP, but with only minor overlap of their epitopes (Kirchhofer et al., 2010), and are therefore ideally suited for engineering orthogonal pairs. To this end, we mutated monomeric enhanced green and cyan fluorescent proteins (mEGFP and mECFP, respectively), which were expected to selectively weaken binding of either of each NB (Figures 1B and S1A). These mEGFP mutants were expressed and purified to homogeneity, and the interaction with EN and MI was quantified by simultaneous label-free and fluorescence real-time solid-phase detection (Figure 1C). Introducing the mutations N198D and Y200F in mEGFP (mEGFPe) together reduced the affinity of MI by ~1000-fold while not affecting binding of EN (Figures 1D and S1B–S1G). The mutation E142K introduced into mECFP (mECFPm) fully abrogated binding of EN, which was previously shown to bind CFP only weakly (Rothbauer et al., 2008). By contrast, the binding affinity of MI to mECFPm compared with mEGFP was only mildly reduced (Figures 1D and S1H). Corresponding non-fluorescent variants of mEGFPe (mXFPe) and mECFPm (mXFPm) were obtained by introducing a Phe at

Figure 2. Orthogonal, high-efficiency cell surface labeling via engineered GFP tags

(A–D) Selectivity was determined by quantifying labeling of mEGFPe-IFNAR1 and mECFPm-IFNAR1, respectively, after labeling with each 10 nM ^{Rho11}EN and ^{DY647}MI (A). (B and C) Overlay of single-molecule trajectories detected in the Rho11 (green) and the DY647 (violet) channels in a cell expressing mEGFPe-IFNAR1 (B) and a cell expressing mCFPm-IFNAR1 (C). (D) Relative number of molecules detected in the Rho11 (green) and the DY647 (purple) channels for labeling different GFP variants.

(E–H) The degree of labeling (DOL) quantified by smFRET from ^{Rho11}NBs to DY647 introduced via a proximal SNAPf-tag (E). (F and G) Overlay of single-molecule trajectories of cell surface SNAPf-mECFPm-IFNAR1 labeled with MI^{Rho11} (F) and SNAPf-mEGFPm-IFNAR1 labeled with EN^{Rho11} (G). Color-coding: blue: Rho11; red: DY647 excited at 640 nm; violet: DY647 excited by FRET. Scale bars: 2 μm. (H) Comparison of the effective DOL obtained for different GFP/NB pairs. Boxplots indicate the data distribution of second and third quartile (box), median (line), mean (square), and 1.5× IQR (whiskers). Each data point represents the analysis from one cell with a minimum of 10 cells measured for each condition. DOL >1 for individual data points can be attributed to the limited localization fidelity (see STAR Methods).

position 66 (Y66F and W66F, respectively) and showed similar binding affinities (Figure S1H). Spectral properties, quantum yield, and brightness as well as the monomeric nature of the parental fluorescent proteins mECFP and mEGFP remained largely unchanged by introducing the mutations (Figures S1I–S1K).

Selective, high-efficiency cell surface labeling by nanobodies EN and MI

For live-cell labeling, EN and MI were produced with an additional C-terminal Cys residue for site-specific conjugation with the photostable fluorescence dyes ATTO 488 (AT488), ATTO Rho11 (Rho11), DY-647P1 (DY647), ATTO 643 (AT643), and DY-752 (DY752), respectively, via maleimide chemistry. As protein precipitation was observed upon labeling with Rho11 and other hydrophobic rhodamine dyes, we included a C-terminal PASylation tag (Thomas and Weber, 2019) downstream of the Cys residue to enhance NB stability. Thus, site-specifically fluorophore-conjugated NBs with a DOL close to 1.0 were achieved for both EN and MI. Using these homogenously labeled NBs, we explored orthogonal labeling via the EN/mEGFPe and MI/mECFPm interaction pairs by single-

molecule localization microscopy in living cells. To this end, mEGFPe and mECFPm, respectively, were fused to the N-terminus of the type I IFN receptor subunit 1 (IFNAR1). Cell surface expression of IFNAR1 is tightly regulated at low densities, and we previously demonstrated its strictly monomeric state in the PM (Wilmes et al., 2015). mEGFPe-IFNAR1 and mECFPm-IFNAR1 were each expressed in HeLa cells and labeled by simultaneous incubation of ^{Rho11}EN and ^{DY647}MI (10 nM each). To minimize background signals caused by non-specific binding to the cover slide glass surface, cells were cultured on substrates coated with poly-L-lysine-graft-polyethylene glycol functionalized with the peptide RGD to allow cell adhesion (You et al., 2014). Labeling specificity was probed by dual-color total internal reflection fluorescence (TIRF) imaging in presence of each 2 nM ^{Rho11}EN and ^{DY647}MI (Figure 2A and Data S1, Video Orthogonal nanobody labeling). Background signals from non-specific NB binding to the coated glass surface remained negligible even in presence of labeled NB in the bulk (Figure S2A). Quantifying the number of molecules detected in each channel confirmed highly selective labeling of mEGFPe-IFNAR1 by ^{Rho11}EN and mECFPm-IFNAR1 by ^{DY647}MI under these conditions (Figures 2B–2D).
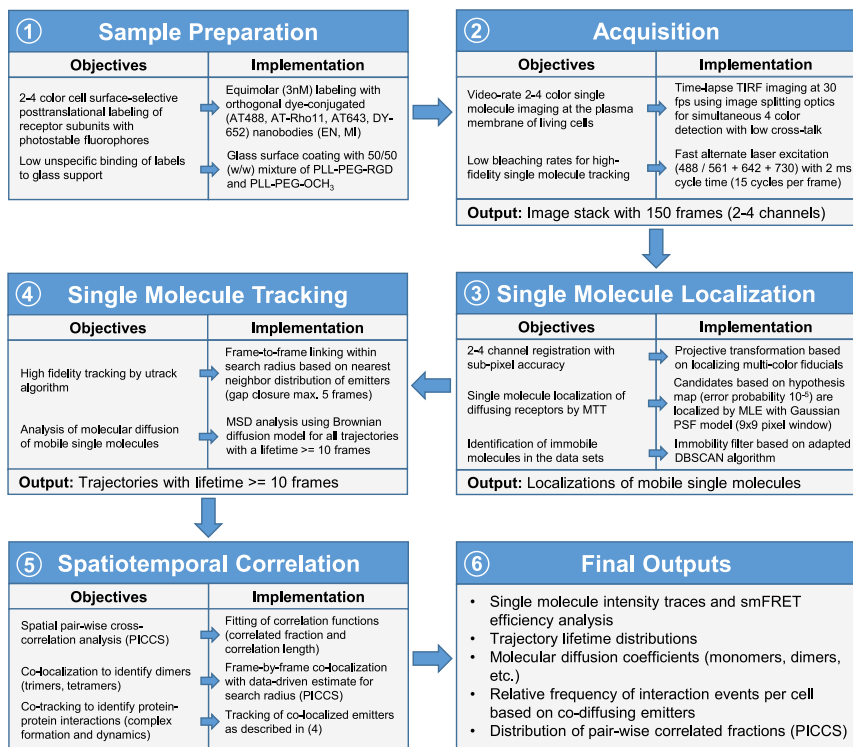
Figure 3. Workflow of multicolor single-molecule imaging and analysis from sample preparation to final data outputs.

face was achieved by addition of a monoclonal anti-MBP IgG. After cell surface labeling with a mixture of [Rho11]EN and [DY647]EN, cells were subjected to time-lapse dual-color single-molecule imaging in the absence and presence of 20 nM anti-MBP. Results from single-molecule diffusion and interaction analyses are summarized in Figure S2. Background binding of NBs to non-transfected HeLa cells was found to be negligible (<0.05 localizations/μm^2) compared to typically 0.3–0.7 localizations/μm^2 for each channel observed for transfected cells that were chosen for analysis (Figures S2A–S2C).

Dimerization was quantified by dual-color co-tracking (spatiotemporal correlation) (Flores-Otero et al., 2014; Koyama-Honda et al., 2005) and by particle image cross-correlation spectroscopy (PICCS) (Semrau et al., 2011). The robustness of co-tracking was explored by systematically varying co-localization precision and minimum length of co-trajectories (Figures S2D and S2E). Since dimerization was only expected in the presence of anti-MBP, these analyses were assessed for minimum signal under these conditions while obtaining maximum dimerization in the presence of anti-MBP. Overall, a minimum trajectory length of 10 consecutive frames in conjunction with a co-localization search radius of 150 nm turned out as a robust tradeoff. False-positive dimers were minimized after filtering immobile molecules, possibly because these signals were in part related to signals from PM-proximal endosomes. Under such optimized conditions, background homodimerization below 1% was observed, compared to >30% homodimerization in the presence of anti-MBP (Figure S2F). By contrast, PICCS analysis yielded a background of >10% homodimerization in the absence of anti-MBP (Figure S2G). With a homodimerization level of >50% obtained in the presence of anti-MBP, a similar change in dimerization was observed compared to co-tracking analysis. Interestingly, a PICCS correlation length of 70 nm was observed upon dimerization with anti-MBP (Figure S2H), which can be interpreted as the effective co-localization precision.

Diffusion properties were quantified by spatiotemporal clustering to identify immobile particles followed by tracking of the mobile fraction. Mean squared displacement (MSD) analysis of single molecule trajectories over a total of 10 frames (320 ms) yielded linear dependence as expected for random diffusion with a mean diffusion constant of 0.135 μm^2/s (Figure S2I). Dimerization by anti-MBP reduced the diffusion constant to an average of 0.08 μm^2/s, with the fraction of dimer identified by co-tracking showing a diffusion constant of 0.06 μm^2/s. Furthermore, a strong

We employed single-molecule Förster resonance energy transfer (smFRET) for quantifying the DOL achieved by NB labeling of target proteins in the PM of live cells. To this end, the SNAPf-tag was fused to the N-terminus of mEGFPe-IFNAR1 and mECFPm-IFNAR1, respectively, which each were expressed in HeLa cells (Figure 2E). After labeling with SNAP-Surface647 as FRET acceptor, NBs labeled with Rho11 were added, and smFRET was quantified by alternating laser excitation (Figures 2F and 2G and Data S1, Video DOL by smFRET). The DOL was determined by comparing the number of acceptor molecules detected upon donor excitation versus the total number of acceptor molecules observed upon direct acceptor excitation (Figure 2H). Very high effective DOL of ~0.8 for MI/mECFPm and ~1.0 for EN/mEGFPe were observed, which were in line with the slightly different binding affinities determined for the two interaction pairs. Very similar DOLs were obtained for the corresponding non-fluorescent GFP variants (Figure 2H).

Co-tracking analysis for robust quantification of protein dimerization in the PM

Well-defined and high-efficiency, orthogonal NB labeling served as foundation for interrogating with high-fidelity diffusion and interaction of receptors in the PM by multicolor SMFM. The overall workflow for sample preparation, multicolor image acquisition, and spatiotemporal single-molecule analyses is summarized in Figure 3. The capabilities of different evaluation approaches of diffusion and interaction analysis were systematically tested using the model transmembrane helix (ALA)$_7$, which was N-terminally fused to mEGFP and maltose binding protein (MBP). Efficient homodimerization of this protein at the cell sur-

increase of the immobile fraction was observed upon dimerization (Figure S2J), highlighting the considerable difference in the diffusion properties of monomers and dimers in the PM.

IFNγ receptor dimerization quantified by dual-color single-molecule co-tracking

For proof-of-concept application, we chose the IFNγ receptor, which is comprised of two subunits, IFNGR1 and IFNGR2 (Bach et al., 1997). IFNγ is a homodimeric agonist, which supposedly recruits two copies of each IFNGR1 and IFNGR2 at the cell surface as predicted by the crystal structures of the extracellular receptor domains in complex with IFNγ (Figure 4A) (Mendoza et al., 2019; Walter et al., 1995). However, pre-assembly of the IFNγ receptor subunits in lipid nanodomains has been proposed (Blouin et al., 2016; Krause et al., 2002, 2006b), and therefore the spatial organization and the stoichiometry of the IFNγ receptor signaling complex in the PM has remained controversial. The extracellular domain (ECD) of IFNGR1 binds IFNγ with nanomolar affinity, while IFNGR2-ECD recognizes IFNγ only when already in complex with IFNGR1-ECD with an affinity in the higher micromolar range (Marsters et al., 1995). Therefore, IFNGR1 and IFNGR2 are considered as "binding" and "accessory" receptor subunits, respectively.

Wild-type HeLa cells endogenously express IFNGR1 and IFNGR2 and are fully responsive to IFNγ (Krause et al., 2006a). To quantify cell surface expression of the endogenous IFNGR, untransfected HeLa cells were incubated with site-specifically fluorescence-labeled IFNγ at saturating concentrations and imaged by TIRF microscopy. Individual signals could be readily discerned with a mean density of 0.55 molecules/μm^2 (Figure S2A). Similar densities have been reported for the related interferon α/β receptor IFNAR (Wilmes et al., 2015), corroborating that single-molecule techniques are well suitable for investigating this class of receptors. To identify potential ligand-independent receptor co-organization in the PM, we first probed for homodimerization of IFNGR1 fused to mXFPm (mXFPm-IFNGR1) by labeling with ^{Rho11}MI and ^{AT643}MI at equimolar concentrations. In the absence of IFNγ, uncorrelated, random diffusion of individual IFNGR1 was observed as confirmed by single-molecule photobleaching and dual-color (co-)tracking analyses (Figure 4B–4D and S3A–S3C and Data S2, Video Homodimerization of IFNGR1). Upon addition of IFNγ, substantial homodimerization of IFNGR1 was observed, which was not detectable in case of a functionally monomeric IFNγ variant (mIFNγ) (Landar et al., 2000) that only binds a single copy of IFNGR1 (Figures 4C and 4D and Data S2, Video Homodimerization of IFNGR1). Similar results were obtained upon co-expression of mXFPe-IFNGR2, which was confirmed at single cell level by labeling with EN conjugated with ATTO488 (^{AT488}EN). Likewise, homodimerization of mXFPe-IFNGR2 was detectable only in the presence of IFNγ (Figure 4E and Data S2, Video Homodimerization of IFNGR2), though substantially lower dimerization levels were observed in line with the much lower affinity of the IFNγ/IFNGR2 interaction. The considerable level of endogenous IFNGR1 identified by staining with labeled IFNγ (see above) was high enough to ensure efficient cytokine binding as co-expression of mXFPm-IFNGR1 did not further enhance homodimerization of IFNGR2. Heterodimerization of IFNGR1 and IFNGR2 was explored by co-expressing mXFPm-IFNGR1 and mXFPe-IFNGR2, which were labeled with ^{Rho11}MI and ^{AT643}EN, respectively. Co-tracking analysis revealed that interaction of IFNGR1 and IFNGR2 only occurred in presence of ligand (Figure 4E, Data S2, Video Heterodimerization of IFNGR1 and IFNGR2). For mIFNγ, somewhat lower levels of heterodimerization were observed compared to IFNγ, which can be explained by the lower probability for detecting dimers in a 1:1 versus a 2:2 IFNGR1:IFNGR2 stoichiometry that can be formed by mIFNγ and IFNγ, respectively, cf. Figure 4A. While these spatiotemporal correlation analyses unambiguously identified receptor homo- and heterodimerization only in the presence of ligand, spatial correlation by PICCS applied to the same dataset yielded a more ambiguous picture. Whereas the correlated fraction clearly increased upon addition of the ligand, a residual correlated fraction was observed in the absence of ligand (Figure S3D). The correlation lengths of 50–100 nm (Figure S3E), however, imply co-organization at length scale beyond molecular dimensions. Furthermore, similar correlation levels were observed for the negative control experiments (cf. Figure S2H), suggesting a background cross-correlation level due to intrinsic heterogeneity of the PM.

IFNγ receptor diffusion and transient arrest correlate with subunit stoichiometry

We extracted the diffusion properties of IFNGR1 and IFNGR2 from single-molecule trajectories in resting cells and after stimulation with monomeric and dimeric IFNγ. In absence of ligand, the vast majority of the receptors (~95%) were mobile (Figures S3G–S3J). A linear MSD with increasing lag time was observed, which yielded similar diffusion constants for both receptor subunits (Figure 4F, S3A, S3B, S3C, and S3F). A substantial decrease of the diffusion constant by ~50% was observed upon addition of IFNγ, which was most pronounced when restricting the analysis to receptor dimers (Figure 4F and S4F). Furthermore, the fraction of immobile particles significantly increased in presence of IFNγ, but not mIFNγ (Figures S3G–S3K). Characteristic transitions between mobile and immobile states were observed (Data S2, Video Transient arrest of IFNGR2 homodimers). Such stimulation-induced temporary arrest of lateral diffusion (STALL) (Suzuki et al., 2007) events could be related to transient partitioning into membrane microdomains related to caveolae-mediated receptor endocytosis, which has been proposed for IFNγ receptor (Blouin et al., 2016; Marchetti et al., 2006). A significantly lower decrease in the diffusion constant and a largely unchanged propensity for STALLing compared to non-stimulated cells was observed in the presence of mIFNγ. Taken together, a stringent correlation of diffusion properties with the stoichiometry of receptor subunits was found by our analysis, supporting a simple model of ligand-induced tetramerization and heterodimerization by IFNγ and mIFNγ, respectively.

smFRET confirms the structural organization of the IFNγ signaling complex

These results suggest IFNγ-induced formation of receptor homo- and heterodimers according the structural model shown in Figure 4A with efficiencies governed by the differential binding affinities of the receptor subunits. To further explore the
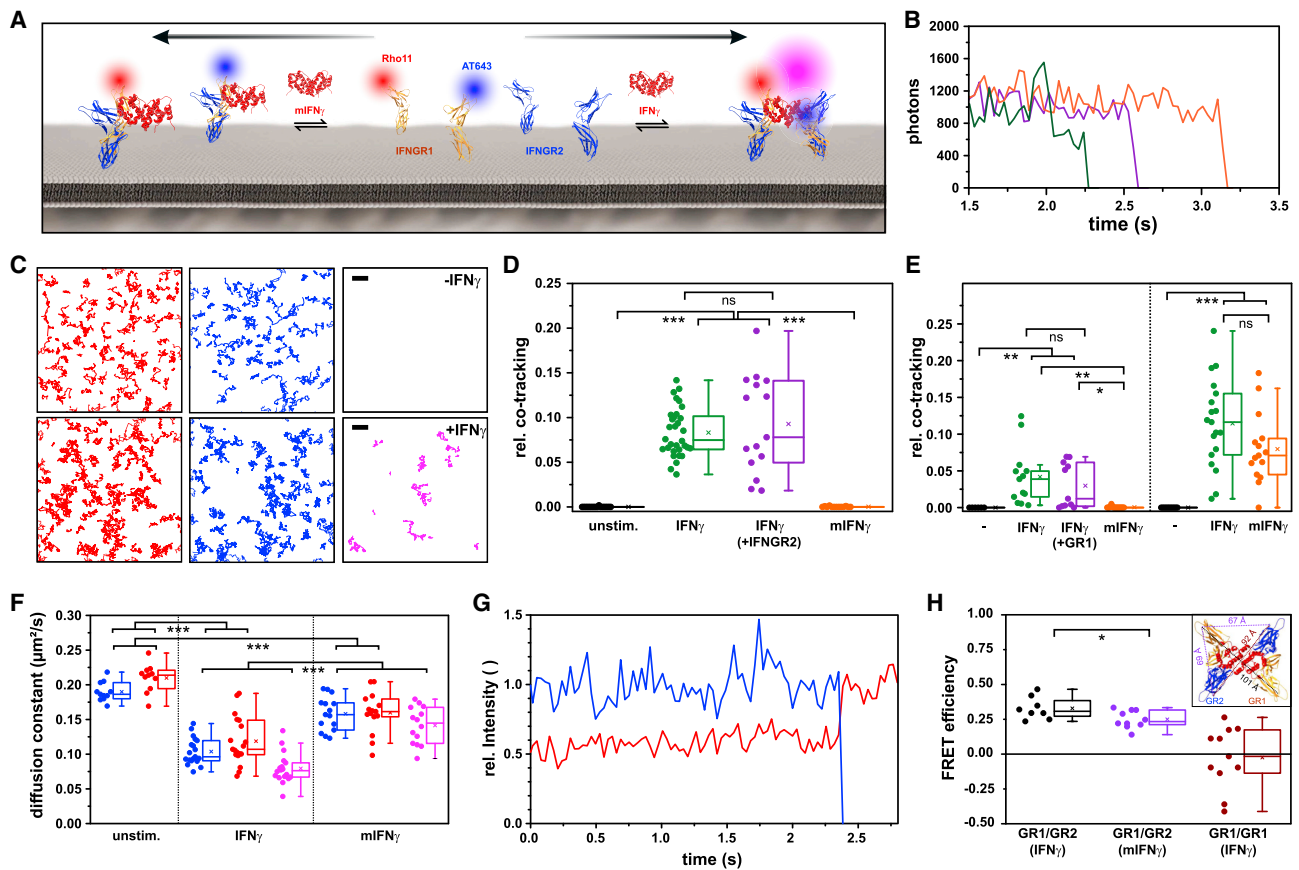
Figure 4. Spatiotemporal organization and dynamics of the IFNγ receptor probed by multicolor single-molecule techniques

(A) Assembly of the IFNγ receptor signaling complex by homo- and heterodimerization of the receptor subunits IFNGR1 (blue) and IFNGR2 (orange). By labeling of mXFPm-IFNGR1 and mXFPe-IFNGR2 via MI and EN, respectively, homo- and heterodimerization was quantified by dual-color co-tracking (exemplified for IFNGR1 homodimerization).

(B) Single-molecule imaging confirmed by single-step photobleaching. Intensities profiles for three representative single-molecule trajectories are shown.

(C) Dual-color single-molecule tracking and co-tracking of IFNGR1 in absence (top) and in presence (bottom) of IFNγ. Trajectories of mXFPm-IFNGR1 labeled with [Rho11]MI (red) and [AT643]MI (blue) and co-trajectories (magenta). Scale bar: 1 μm.

(D) Homodimerization of IFNGR1 in the absence of ligand and after stimulation with IFNγ (green) or with mIFNγ (orange) as quantified by dual-color co-tracking. Homodimerization by IFNγ was also tested upon co-transfection of IFNGR2 (purple).

(E) Homodimerization of mXFPe-IFNGR2 (left) and heterodimerization of mXFPm-IFNGR1/mXFPe-IFNGR2 (right). Homodimerization by IFNγ was also tested upon co-transfection of IFNGR1 (purple).

(F) Diffusion constants of IFNGR1 (blue) and IFNGR2 (red) in the absence and presence of IFNγ and mIFNγ, respectively, obtained from single-molecule trajectories by mean square displacement (MSD) analysis (cf. Figure S4). Diffusion constants of strictly detected receptors dimers for comparison (magenta).

(G and H) Structural organization of IFNGR homo and heterodimers in the plasma membrane analyzed by smFRET (G) Typical intensity profile of an mXFPm-IFNGR1/mXFPe-IFNGR2 heterodimer labeled with [Rho11]MI (red, donor) and [AT643]EN (blue, acceptor). Acceptor photobleaching is accompanied by an increase in donor intensity. (H) Comparison of FRET efficiencies *E* observed for homo- and heterodimerization of IFNGR1 and IFNGR2 determined from the donor recovery. Inset: top view of the IFNγ receptor complex (PDB: 6E3K) indicating the distances between the N-termini of IFNGR1 (GR1) and IFNGR2 (GR2) homo- and heterodimers. Boxplots indicate the data distribution of second and third quartile (box), median (line), mean (cross), and 1.5× IQR (whiskers). Each data point represents the analysis from one cell in (D)–(F) and from one trajectory in (H). Statistical analysis by unpaired student's t test. Significances are indicated by asterisks (ns: $p > 0.05$, *: $p \leq 0.05$, **: $p \leq 0.01$, ***$p \leq 0.001$).

structural organization of IFNGR1 and IFNGR2 in the homo- and heterodimers formed at the PM, we estimated the distances between receptor subunits by smFRET. In case of IFNGR1/IFNGR2 heterodimers, significant increase in the donor signal was observed upon acceptor photobleaching (Figure 4G and Data S2, Video smFRET in individual IFNGR1-IFNGR2 heterodimers). An average FRET efficiency of ~25% was obtained from this analysis (Figure 4H). Given the theoretical Förster radius of

6.9 nm for the Rho11/AT643 pair, this FRET efficiency corresponds to a distance of ~8.3 nm. A similar FRET efficiency was obtained for IFNGR1/IFNGR2 heterodimers formed by mIFNγ (Figure 4H). These results are in line with the distance of ~7 nm between the N-termini in the *cis*- and the *trans*-heterodimers predicted by the crystal structure (Mendoza et al., 2019) (inset of Figure 4H) when taking into account the additional 1–1.5 nm distance caused by the mXFP-tags and the NBs. By

contrast, FRET was not detectable for homodimeric IFNGR1 complexes, for which substantially larger distance of 10.1 nm between the N-termini are expected from the crystal structure (Figure 4H).

Simultaneous homo- and heterodimerization resolved by multicolor SMFM

These results clearly rule out pre-assembly of the IFNγ receptor subunits, but rather establish IFNγ-induced homo- and heterodimerization of IFNGR1 and IFNGR2. To directly visualize and quantify the formation of multimeric IFNGR1/IFNGR2 complexes, we applied four-color SMFM. For this purpose, HeLa cells co-expressing mXFPm-IFNGR1 and mXFPe-IFNGR2 were labeled with ^{AT488}MI, ^{Rho11}MI, ^{AT643}EN, and ^{DY752}EN (Figure 5A) at equimolar concentrations and subjected to four-color SMFM. Under these labeling conditions, minimum bias of signal intensities by FRET are expected (Figure 5A). By applying alternating laser excitation (Figures S4A and S4B), robust four-color SMFM was achieved at video rates with sufficient signal intensity and similar number of localized molecules in all four channels (Figures S4C–S4E). Thus, four-color single-molecule tracking and co-tracking with high fidelity was achieved (Figure 5B and Data S3, Video Four-color single-molecule imaging). Pairwise dual-color co-tracking analysis confirmed ligand-induced homo- and heterodimerization of IFNGR1 and IFNGR2 (Figure 5C, Data S3, Video Four-color co-tracking). These results were confirmed by spatial cross-correlation using PICCS leading to significant pairwise correlated fractions (Figures S4F and S4G). Strikingly, complexes labeled in three different colors were detectable, which unambiguously confirm simultaneous formation of homo- and heterodimers (Figure 5D). While homodimers of IFNGR1 in complex with IFNGR2 were rather abundant, trimers comprising two copies of IFNGR2 were not detectable, in line with the cooperativity of the IFNGR1-IFNGR2 interaction. These observations support our model of ligand-induced homo- and heterodimerization of IFNGR1 and IFNGR2, which is governed by the differential ligand binding affinities of the receptor subunits. The overall levels of homo- and heterodimerization observed in four-color SMFM experiments (Figure 5E) very well matched the results from sequential dual-color imaging. These experiments highlight the key capability to simultaneously quantify receptor homo- and heterodimerization in the PM by four-color SMFM.

DISCUSSION

Unraveling the spatial organization of cell surface receptors is a key prerequisite for a mechanistic understanding of the activation and the spatiotemporal regulation of cellular signaling. Emerging models of cytokine receptor signaling suggest pre-dimerized or pre-clustered receptor subunits in the absence of ligand (Brooks et al., 2014; Brown et al., 2005; Constantinescu et al., 2001; Low-Nam et al., 2011; Purba et al., 2017; Stroud and Wells, 2004; Tenhumberg et al., 2006; Yang et al., 2007; Zaks-Zilberman et al., 2008), but receptor pre-organization in the PM remains controversial because reliable quantification has been lacking so far (Atanasova and Whitty, 2012; Baumgart et al., 2016; Feher et al., 2019). Similar concepts have emerged

for other classes of receptors including G-protein-coupled receptors (Ferre et al., 2014; Kasai and Kusumi, 2014; Lambert and Javitch, 2014; Moller et al., 2020). We have here established a comprehensive toolbox for analyzing receptor homo- and heterodimerization in the PM of live cells by SMFM. Based on engineering specific, high-affinity nanobody-GFP binding pairs, orthogonal labeling of proteins in the PM of living cells with very high fidelity and efficiency was achieved as required for reliable, long-term multicolor SMFM. In conjunction with a robust and experimentally validated toolbox for spatiotemporal single-molecule analysis, this approach enabled to unambiguously quantify stoichiometries and structural organization of signaling complexes in the PM of live cells with minimum bias from receptors in intracellular membranes.

Rigorous application of these tools clearly rule out pre-dimerization of the IFNγ receptor subunits, which has been previously suggested based on ensemble FRET and bioluminescence resonance energy transfer detection techniques (Blouin et al., 2016; Krause et al., 2002, 2006b). These approaches based on genetically encoded proteins could not discriminate between receptors in the PM and in endosomal compartments, which often strongly enrich overexpressed PM proteins. By contrast, the application of live-cell single-molecule TIRF microscopy in conjunction with efficient extracellular labeling with photostable fluorescent dyes allowed highly selective detection of receptors localized in the PM with minimum background from endocytosed receptors. Efficient identification and long-term observation of receptor dimers allowed an estimate of intermolecular distances by smFRET, thus providing information on the structural organization of receptor subunits within a signaling complex in the PM of live cells. While we cannot rule out partitioning into lipid domains, these results point to protein-protein interactions being responsible for the observed co-diffusion. Dimerization efficiency and dynamics (Freed et al., 2017; Gorby et al., 2020; Kim et al., 2017; Martinez-Fabregas et al., 2019; Mitra et al., 2015; Mohan et al., 2019) as well as the architecture of signaling complexes (Mohan et al., 2019; Moraga et al., 2015) have emerged as key determinants of cytokine activities and specificities (Spangler et al., 2015). Reliable quantification of receptor homo- and heterodimerization as well as intermolecular distances thus will provide the basis to systematically engineer novel agonists for therapeutic applications.

Because of the low concentrations of nanobodies required for efficient cell surface labeling, these experiments can be conducted under conditions that maintain high DOL with minimum background, even for cell surface proteins with high turnover. However, NB labeling is reversible, which may have disadvantages for long-term imaging applications, e.g., for tracking endosomal receptor trafficking. Therefore, this approach perfectly complements covalent posttranslational labeling via the SNAP-tag (Keppler et al., 2004) or the HaloTag (Los et al., 2008), which provide the advantage of irreversible dye conjugation, but do yield lower DOL (Schlichthaerle et al., 2019; Wilmes et al., 2015). NB-based labeling can be readily combined with these and other high-affinity, non-covalent labeling techniques (Doh et al., 2018; Gotzke et al., 2019) to simultaneously resolve diffusion and interactions of multiple cell surface receptors. We have here demonstrated multiplexed analysis of diffusion and
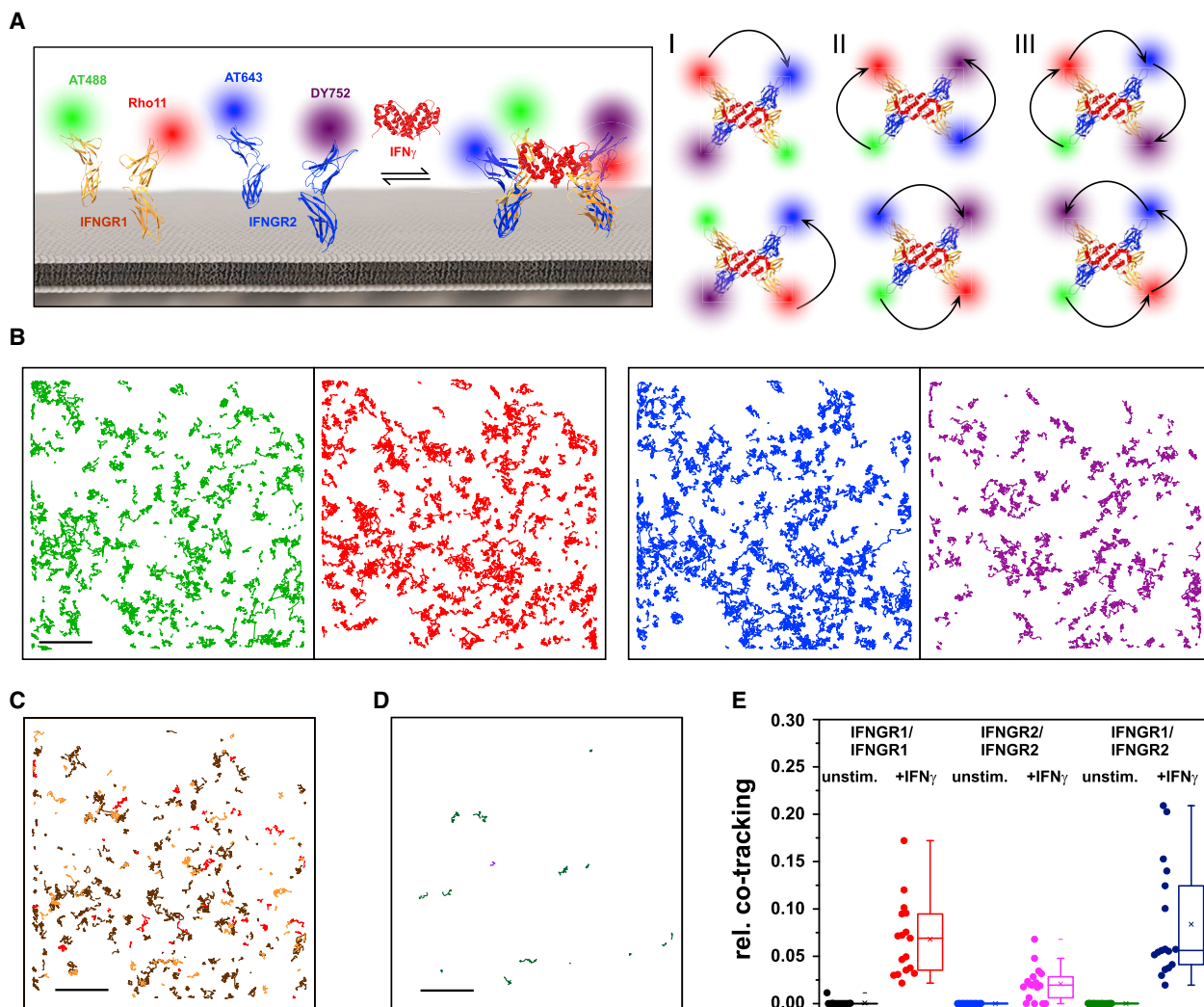
Figure 5. Simultaneous detection of IFNGR1 and IFNGR2 homo- and heterodimerization by four-color single-molecule imaging

(A) Cartoon of the assays (left) and possible combinations of four different dyes to label homo- and heterodimers (I–III). Arrows indicate dye pairs and distances allowing significant FRET.

(B) Single-molecule trajectories from a representative four-color imaging experiment of a HeLa cells co-expressing mXFPm-IFNGR1, which was labeled with ^{AT488}MI (green) and ^{Rho11}MI (red), and mXFPe-IFNGR2, which was labeled with ^{AT643}EN (blue) and ^{DY752}EN (purple). Scale bar: 5 μm.

(C) Dual-color co-trajectories corresponding to IFNGR1 homodimers (orange), IFNGR2 homodimers (red), and IFNGR1/IFNGR2 heterodimers (brown). Scale bar: 5 μm.

(D) Triple-color co-trajectories corresponding to IFNGR1 homodimers in complex with IFNGR2 (dark green) and IFNGR2 homodimers in complex with IFNGR1 (purple). Scale bar: 5 μm.

(E) Homo- and heterodimerization obtained from dual-color co-tracking analyses. The boxplot indicates the data distribution of second and third quartile (box), median (line), mean (square), and whiskers (1.5× IQR). Each data point represents the analysis from one cell with a minimum of 10 cells measured for each condition.

interaction at the single molecule level with four colors, which will enable to study the cross talk of such multi-receptor systems. However, the application of orthogonal NB labeling is not limited to cell surface receptors. Since different spectral variants are involved in the EN/mEGFPe and MI/mECFPm pairs, dual-color nanobody labeling in fixed cells can be readily envisaged, which is increasingly popular for superresolution imaging including stochastic optical reconstruction microscopy (Ries et al., 2012; Virant et al., 2018), DNA point accumulation in nanoscale topology

(Schlichthaerle et al., 2019), and stimulated emission depletion microscopy (Cramer et al., 2019).

Limitations of the study

Single-molecule co-tracking for analyzing receptor assembly in the PM is ideally suited for cell surface densities below 1 μm^{-2}, but much less powerful at significantly higher expression levels. A potential workaround is a technique termed "thinning out clusters while conserving stoichiometry of labeling" (TOCCSL) that

combines dual-color single-molecule imaging with local photobleaching (Ruprecht et al., 2010). As SMT in the PM requires video rate time resolution, overall observation times of individual cells are limited to a few 10 s due to photobleaching. Further challenges arise from the turnover of cell surface receptors by endocytosis, which is often induced by stimulation with the ligand. Owing to sequential imaging of individual cells, endocytosis and other cellular responses may systematically bias receptor dynamics. Likewise, strong changes in receptor diffusion properties, which can also be related to endocytosis, can bias the outcome, which is fundamentally based on the mobility of signaling complexes. To minimize these potential biases, imaging at room temperature rather than 37°C is recommended.

STAR★METHODS

Detailed methods are provided in the online version of this paper and include the following:

- KEY RESOURCES TABLE
- RESOURCE AVAILABILITY
  - Lead contact
  - Materials availability
  - Data and code availability
- EXPERIMENTAL MODEL AND SUBJECT DETAILS
  - HeLa cells
- METHOD DETAILS
  - Plasmids
  - Expression and purification of NBs and GFP variants
  - Simultaneous TIRF spectroscopy and reflectance interference detection
  - Fluorescence spectroscopy
  - Fluorescence lifetime measurements
  - Live-cell labeling
  - Single-molecule localization microscopy
- QUANTIFICATION AND STATISTICAL ANALYSIS
  - Single molecule data evaluation
  - Particle image cross-correlation spectroscopy (PICCS)
  - Degree of labeling (DOL)
  - Mean squared displacement analysis
  - Single molecule FRET analysis
  - Statistical analysis

SUPPLEMENTAL INFORMATION

Supplemental information can be found online at https://doi.org/10.1016/j.crmeth.2022.100165.

AUTHOR CONTRIBUTIONS

J.P., O.B., J.S.B., and R.K. conceived the project together with C.Y., M.R.W., and U.R. O.B. and F.E. designed and performed protein engineering and char-
acterization experiments. O.B., F.E., and H.K. produced and labeled proteins. J.S.B. and O.B. designed and performed live-cell single-molecule imaging experiments with support from S.W., R.K., and M.R.W. C.P.R conceived and programmed evaluation software. J.S.B. and O.B. performed image analysis with support from C.P.R. O.B., J.S.B., R.K., and J.P. wrote the manuscript with contributions from all authors.

REFERENCES

Albrecht, D., Winterflood, C.M., and Ewers, H. (2015). Dual color single particle tracking via nanobodies. Methods Appl. Fluoresc. *3*, 024001.

Asher, W.B., Geggier, P., Holsey, M.D., Gilmore, G.T., Pati, A.K., Meszaros, J., Terry, D.S., Mathiasen, S., Kaliszewski, M.J., McCauley, M.D., et al. (2021). Single-molecule FRET imaging of GPCR dimers in living cells. Nat. Methods *18*, 397–405.

Atanasova, M., and Whitty, A. (2012). Understanding cytokine and growth factor receptor activation mechanisms. Crit. Rev. Biochem. Mol. Biol. *47*, 502–530.

Bach, E.A., Aguet, M., and Schreiber, R.D. (1997). The IFN gamma receptor: a paradigm for cytokine receptor signaling. Annu. Rev. Immunol. *15*, 563–591.

Baumgart, F., Arnold, A.M., Leskovar, K., Staszek, K., Folser, M., Weghuber, J., Stockinger, H., and Schutz, G.J. (2016). Varying label density allows artifact-free analysis of membrane-protein nanoclusters. Nat. Methods *13*, 661–664.

Bernardino de la Serna, J., Schutz, G.J., Eggeling, C., and Cebecauer, M. (2016). There is no simple model of the plasma membrane organization. Front. Cell Dev. Biol. *4*, 106.

Blouin, C.M., Hamon, Y., Gonnord, P., Boularan, C., Kagan, J., Viaris de Lesegno, C., Ruez, R., Mailfert, S., Bertaux, N., Loew, D., et al. (2016). Glycosylation-Dependent IFN-gammaR partitioning in lipid and actin nanodomains is critical for JAK activation. Cell *166*, 920–934.

Brameshuber, M., and Schutz, G.J. (2012). Detection and quantification of biomolecular association in living cells using single-molecule microscopy. Methods Enzymol. *505*, 159–186.

Brooks, A.J., Dai, W., O'Mara, M.L., Abankwa, D., Chhabra, Y., Pelekanos, R.A., Gardon, O., Tunny, K.A., Blucher, K.M., Morton, C.J., et al. (2014). Mechanism of activation of protein kinase JAK2 by the growth hormone receptor. Science *344*, 1249783.

Brown, R.J., Adams, J.J., Pelekanos, R.A., Wan, Y., McKinstry, W.J., Palethorpe, K., Seeber, R.M., Monks, T.A., Eidne, K.A., Parker, M.W., et al. (2005). Model for growth hormone receptor activation based on subunit rotation within a receptor dimer. Nat. Struct. Mol. Biol. *12*, 814–821.

Cambi, A., and Lidke, D.S. (2012). Nanoscale membrane organization: where biochemistry meets advanced microscopy. ACS Chem. Biol. *7*, 139–149.

Constantinescu, S.N., Keren, T., Socolovsky, M., Nam, H., Henis, Y.I., and Lodish, H.F. (2001). Ligand-independent oligomerization of cell-surface erythropoietin receptor is mediated by the transmembrane domain. Proc. Natl. Acad. Sci. U S A *98*, 4379–4384.

Cramer, K., Bolender, A.L., Stockmar, I., Jungmann, R., Kasper, R., and Shin, J.Y. (2019). Visualization of bacterial protein complexes labeled with fluorescent proteins and nanobody binders for STED microscopy. Int. J. Mol. Sci. *20*, 3376.

da Rocha-Azevedo, B., Lee, S., Dasgupta, A., Vega, A.R., de Oliveira, L.R., Kim, T., Kittisopikul, M., Malik, Z.A., and Jaqaman, K. (2020). Heterogeneity

in VEGF receptor-2 mobility and organization on the endothelial cell surface leads to diverse models of activation by VEGF. Cell Rep. *32*, 108187.

Doh, J.K., White, J.D., Zane, H.K., Chang, Y.H., Lopez, C.S., Enns, C.A., and Beatty, K.E. (2018). VIPER is a genetically encoded peptide tag for fluorescence and electron microscopy. Proc. Natl. Acad. Sci. U S A *115*, 12961–12966.

Feher, K., Halstead, J.M., Goyette, J., and Gaus, K. (2019). Can single molecule localization microscopy detect nanoclusters in T cells? Curr. Opin. Chem. Biol. *51*, 130–137.

Ferre, S., Casado, V., Devi, L.A., Filizola, M., Jockers, R., Lohse, M.J., Milligan, G., Pin, J.P., and Guitart, X. (2014). G protein-coupled receptor oligomerization revisited: functional and pharmacological perspectives. Pharmacol. Rev. *66*, 413–434.

Flores-Otero, J., Ahn, K.H., Delgado-Peraza, F., Mackie, K., Kendall, D.A., and Yudowski, G.A. (2014). Ligand-specific endocytic dwell times control functional selectivity of the cannabinoid receptor 1. Nat. Commun. *5*, 4589.

Freed, D.M., Bessman, N.J., Kiyatkin, A., Salazar-Cavazos, E., Byrne, P.O., Moore, J.O., Valley, C.C., Ferguson, K.M., Leahy, D.J., Lidke, D.S., et al. (2017). EGFR ligands differentially stabilize receptor dimers to specify signaling kinetics. Cell *171*, 683–695 e618.

Garcia-Parajo, M.F., Cambi, A., Torreno-Pina, J.A., Thompson, N., and Jacobson, K. (2014). Nanoclustering as a dominant feature of plasma membrane organization. J. Cell Sci *127*, 4995–5005.

Gavutis, M., Lata, S., Lamken, P., Müller, P., and Piehler, J. (2005). Lateral ligand-receptor interactions on membranes probed by simultaneous fluorescence-interference detection. Biophys. J. *88*, 4289–4302.

Gorby, C., Sotolongo Bellon, J., Wilmes, S., Warda, W., Pohler, E., Fyfe, P.K., Cozzani, A., Ferrand, C., Walter, M.R., Mitra, S., et al. (2020). Engineered IL-10 variants elicit potent immunomodulatory effects at low ligand doses. Sci. Signal. *13*, eabc0653.

Gotzke, H., Kilisch, M., Martinez-Carranza, M., Sograte-Idrissi, S., Rajavel, A., Schlichthaerle, T., Engels, N., Jungmann, R., Stenmark, P., Opazo, F., et al. (2019). The ALFA-tag is a highly versatile tool for nanobody-based bioscience applications. Nat. Commun. *10*, 4403.

Grecco, H.E., Schmick, M., and Bastiaens, P.I. (2011). Signaling from the living plasma membrane. Cell *144*, 897–909.

Honigmann, A., and Pralle, A. (2016). Compartmentalization of the cell membrane. J. Mol. Biol. *428*, 4739–4748.

Jaqaman, K., Loerke, D., Mettlen, M., Kuwata, H., Grinstein, S., Schmid, S.L., and Danuser, G. (2008). Robust single-particle tracking in live-cell time-lapse sequences. Nat. Methods *5*, 695–702.

Kasai, R.S., and Kusumi, A. (2014). Single-molecule imaging revealed dynamic GPCR dimerization. Curr. Opin. Cell Biol *27*, 78–86.

Kasai, R.S., Suzuki, K.G., Prossnitz, E.R., Koyama-Honda, I., Nakada, C., Fujiwara, T.K., and Kusumi, A. (2011). Full characterization of GPCR monomer-dimer dynamic equilibrium by single molecule imaging. J. Cell Biol. *192*, 463–480.

Keppler, A., Pick, H., Arrivoli, C., Vogel, H., and Johnsson, K. (2004). Labeling of fusion proteins with synthetic fluorophores in live cells. Proc. Natl. Acad. Sci. U S A *101*, 9955–9959.

Kim, A.R., Ulirsch, J.C., Wilmes, S., Unal, E., Moraga, I., Karakukcu, M., Yuan, D., Kazerounian, S., Abdulhay, N.J., King, D.S., et al. (2017). Functional selectivity in cytokine signaling revealed through a pathogenic EPO mutation. Cell *168*, 1053–1064 e1015.

Kinkhabwala, A., and Bastiaens, P.I. (2010). Spatial aspects of intracellular information processing. Curr. Opin. Genet. Dev. *20*, 31–40.

Kirchhofer, A., Helma, J., Schmidthals, K., Frauer, C., Cui, S., Karcher, A., Pellis, M., Muyldermans, S., Casas-Delucchi, C.S., Cardoso, M.C., et al. (2010). Modulation of protein properties in living cells using nanobodies. Nat. Struct. Mol. Biol. *17*, 133–138.

Koyama-Honda, I., Ritchie, K., Fujiwara, T., Iino, R., Murakoshi, H., Kasai, R.S., and Kusumi, A. (2005). Fluorescence imaging for monitoring the colocalization of two single molecules in living cells. Biophys. J. *88*, 2126–2136.

Krause, C.D., He, W., Kotenko, S., and Pestka, S. (2006a). Modulation of the activation of Stat1 by the interferon-gamma receptor complex. Cell Res. *16*, 113–123.

Krause, C.D., Lavnikova, N., Xie, J., Mei, E., Mirochnitchenko, O.V., Jia, Y., Hochstrasser, R.M., and Pestka, S. (2006b). Preassembly and ligand-induced restructuring of the chains of the IFN-gamma receptor complex: the roles of Jak kinases, Stat1 and the receptor chains. Cell Res. *16*, 55–69.

Krause, C.D., Mei, E., Xie, J., Jia, Y., Bopp, M.A., Hochstrasser, R.M., and Pestka, S. (2002). Seeing the light: preassembly and ligand-induced changes of the interferon gamma receptor complex in cells. Mol. Cell Proteomics *1*, 805–815.

Kusumi, A., Fujiwara, T.K., Chadda, R., Xie, M., Tsunoyama, T.A., Kalay, Z., Kasai, R.S., and Suzuki, K.G. (2012). Dynamic organizing principles of the plasma membrane that regulate signal transduction: commemorating the fortieth anniversary of Singer and Nicolson's fluid-mosaic model. Annu. Rev. Cell Dev. Biol. *28*, 215–250.

Kusumi, A., Tsunoyama, T.A., Hirosawa, K.M., Kasai, R.S., and Fujiwara, T.K. (2014). Tracking single molecules at work in living cells. Nat. Chem. Biol. *10*, 524–532.

Lambert, N.A., and Javitch, J.A. (2014). CrossTalk opposing view: weighing the evidence for class A GPCR dimers, the jury is still out. J. Physiol. *592*, 2443–2445.

Landar, A., Curry, B., Parker, M.H., DiGiacomo, R., Indelicato, S.R., Nagabhushan, T.L., Rizzi, G., and Walter, M.R. (2000). Design, characterization, and structure of a biologically active single- chain mutant of human IFN-gamma. J. Mol. Biol. *299*, 169–179.

Lata, S., and Piehler, J. (2005). Stable and functional immobilization of histidine-tagged proteins via multivalent chelator head-groups on a molecular poly(ethylene glycol) brush. Anal. Chem. *77*, 1096–1105.

Los, G.V., Encell, L.P., McDougall, M.G., Hartzell, D.D., Karassina, N., Zimprich, C., Wood, M.G., Learish, R., Ohana, R.F., Urh, M., et al. (2008). HaloTag: a novel protein labeling technology for cell imaging and protein analysis. ACS Chem. Biol. *3*, 373–382.

Low-Nam, S.T., Lidke, K.A., Cutler, P.J., Roovers, R.C., van Bergen en Henegouwen, P.M., Wilson, B.S., and Lidke, D.S. (2011). ErbB1 dimerization is promoted by domain co-confinement and stabilized by ligand binding. Nat. Struct. Mol. Biol. *18*, 1244–1249.

Marchetti, M., Monier, M.N., Fradagrada, A., Mitchell, K., Baychelier, F., Eid, P., Johannes, L., and Lamaze, C. (2006). Stat-mediated signaling induced by type I and type II interferons (IFNs) is differentially controlled through lipid microdomain association and clathrin-dependent endocytosis of IFN receptors. Mol. Biol. Cell *17*, 2896–2909.

Marsters, S.A., Pennica, D., Bach, E., Schreiber, R.D., and Ashkenazi, A. (1995). Interferon gamma signals via a high-affinity multisubunit receptor complex that contains two types of polypeptide chain. Proc. Natl. Acad. Sci. U S A *92*, 5401–5405.

Martinez-Fabregas, J., Wilmes, S., Wang, L., Hafer, M., Pohler, E., Lokau, J., Garbers, C., Cozzani, A., Fyfe, P.K., Piehler, J., et al. (2019). Kinetics of cytokine receptor trafficking determine signaling and functional selectivity. eLife *8*, e49314.

Mendoza, J.L., Escalante, N.K., Jude, K.M., Sotolongo Bellon, J., Su, L., Horton, T.M., Tsutsumi, N., Berardinelli, S.J., Haltiwanger, R.S., Piehler, J., et al. (2019). Structure of the IFNgamma receptor complex guides design of biased agonists. Nature *567*, 56–60.

Michalet, X. (2010). Mean square displacement analysis of single-particle trajectories with localization error: Brownian motion in an isotropic medium. Phys. Rev. E Stat. Nonlin. Soft Matter Phys. *82*, 041914.

Mitra, S., Ring, A.M., Amarnath, S., Spangler, J.B., Li, P., Ju, W., Fischer, S., Oh, J., Spolski, R., Weiskopf, K., et al. (2015). Interleukin-2 activity can be fine tuned with engineered receptor signaling clamps. Immunity *42*, 826–838.

Mohan, K., Ueda, G., Kim, A.R., Jude, K.M., Fallas, J.A., Guo, Y., Hafer, M., Miao, Y., Saxton, R.A., Piehler, J., et al. (2019). Topological control of cytokine

receptor signaling induces differential effects in hematopoiesis. Science *364*, eaav7532.

Möller, J., Isbilir, A., Sungkaworn, T., Osberg, B., Karathanasis, C., Sunkara, V., Grushevskyi, E.O., Bock, A., Annibale, P., Heilemann, M., et al. (2020). Single-molecule analysis reveals agonist-specific dimer formation of micro-opioid receptors. Nat. Chem. Biol. *16*, 946–954.

Moraga, I., Spangler, J., Mendoza, J.L., and Garcia, K.C. (2014). Multifarious determinants of cytokine receptor signaling specificity. Adv. Immunol. *121*, 1–39.

Moraga, I., Wernig, G., Wilmes, S., Gryshkova, V., Richter, C.P., Hong, W.J., Sinha, R., Guo, F., Fabionar, H., Wehrman, T.S., et al. (2015). Tuning cytokine receptor signaling by Re-orienting dimer geometry with surrogate ligands. Cell *160*, 1196–1208.

Niewidok, B., Igaev, M., Pereira da Graca, A., Strassner, A., Lenzen, C., Richter, C.P., Piehler, J., Kurre, R., and Brandt, R. (2018). Single-molecule imaging reveals dynamic biphasic partition of RNA-binding proteins in stress granules. J. Cell Biol. *217*, 1303–1318.

Platonova, E., Winterflood, C.M., and Ewers, H. (2015). A simple method for GFP- and RFP-based dual color single-molecule localization microscopy. ACS Chem. Biol. *10*, 1411–1416.

Purba, E.R., Saita, E.I., and Maruyama, I.N. (2017). Activation of the EGF receptor by ligand binding and oncogenic mutations: the "rotation model". Cells *6*, 13.

Rieger, B., and Stallinga, S. (2014). The lateral and axial localization uncertainty in super-resolution light microscopy. ChemPhysChem *15*, 664–670.

Ries, J., Kaplan, C., Platonova, E., Eghlidi, H., and Ewers, H. (2012). A simple, versatile method for GFP-based super-resolution microscopy via nanobodies. Nat. Methods *9*, 582–584.

Rothbauer, U., Zolghadr, K., Muyldermans, S., Schepers, A., Cardoso, M.C., and Leonhardt, H. (2008). A versatile nanotrap for biochemical and functional studies with fluorescent fusion proteins. Mol. Cell. Proteomics *7*, 282–289.

Rousseeuw, P.J., and Leroy, A.M. (1987). Outlier diagnostics. In Robust Regression and Outlier Detection, P.J. Rousseeuw and A.M. Leroy, eds. (Wiley), pp. 216–247.

Ruprecht, V., Brameshuber, M., and Schutz, G.J. (2010). Two-color single molecule tracking combined with photobleaching for the detection of rare molecular interactions in fluid biomembranes. Soft Matter *6*, 568–581.

Sander, J., Ester, M., Kriegel, H.P., and Xu, X.W. (1998). Density-based clustering in spatial databases: the algorithm GDBSCAN and its applications. Data Mining Knowledge Discov. *2*, 169–194.

Schlichthaerle, T., Strauss, M., Schueder, F., Auer, A., Nijmeijer, B., Kueblbeck, M., Jimenez Sabinina, V., Thevathasan, J., Ries, J., Ellenberg, J., et al. (2019). Direct visualization of single nuclear pore complex proteins using genetically-encoded probes for DNA-PAINT. Angew. Chem. Int. Ed. Engl. *58*, 13004–13008.

Semrau, S., Holtzer, L., Gonzalez-Gaitan, M., and Schmidt, T. (2011). Quantification of biological interactions with particle image cross-correlation spectroscopy (PICCS). Biophys. J. *100*, 1810–1818.

Serge, A., Bertaux, N., Rigneault, H., and Marguet, D. (2008). Dynamic multiple-target tracing to probe spatiotemporal cartography of cell membranes. Nat. Methods *5*, 687–694.

Snyder, G.E., Sakamoto, T., Hammer, J.A., 3rd, Sellers, J.R., and Selvin, P.R. (2004). Nanometer localization of single green fluorescent proteins: evidence that myosin V walks hand-over-hand via telemark configuration. Biophys. J. *87*, 1776–1783.

Spangler, J.B., Moraga, I., Mendoza, J.L., and Garcia, K.C. (2015). Insights into cytokine-receptor interactions from cytokine engineering. Annu. Rev. Immunol. *33*, 139–167.

Stone, M.B., Shelby, S.A., and Veatch, S.L. (2017). Super-resolution microscopy: shedding light on the cellular plasma membrane. Chem. Rev. *117*, 7457–7477.

Stroud, R.M., and Wells, J.A. (2004). Mechanistic diversity of cytokine receptor signaling across cell membranes. Sci. STKE *2004*, re7.

Suzuki, K.G., Fujiwara, T.K., Edidin, M., and Kusumi, A. (2007). Dynamic recruitment of phospholipase C gamma at transiently immobilized GPI-anchored receptor clusters induces IP3-Ca2+ signaling: single-molecule tracking study 2. J. Cell Biol. *177*, 731–742.

Tenhumberg, S., Schuster, B., Zhu, L., Kovaleva, M., Scheller, J., Kallen, K.J., and Rose-John, S. (2006). gp130 dimerization in the absence of ligand: preformed cytokine receptor complexes. Biochem. Biophys. Res. Commun. *346*, 649–657.

Thomas, O.S., and Weber, W. (2019). Overcoming physiological barriers to nanoparticle delivery-are we there yet? Front. Bioeng. Biotechnol. *7*, 415.

Thompson, R.E., Larson, D.R., and Webb, W.W. (2002). Precise nanometer localization analysis for individual fluorescent probes. Biophys. J. *82*, 2775–2783.

Verboven, S., and Hubert, M. (2005). LIBRA: a MATLAB library for robust analysis. Chemometrics Intell. Lab. Syst. *75*, 127–136.

Virant, D., Traenkle, B., Maier, J., Kaiser, P.D., Bodenhofer, M., Schmees, C., Vojnovic, I., Pisak-Lukats, B., Endesfelder, U., and Rothbauer, U. (2018). A peptide tag-specific nanobody enables high-quality labeling for dSTORM imaging. Nat. Commun. *9*, 930.

Vogelsang, J., Kasper, R., Steinhauer, C., Person, B., Heilemann, M., Sauer, M., and Tinnefeld, P. (2008). A reducing and oxidizing system minimizes photobleaching and blinking of fluorescent dyes. Angew. Chem. Int. Ed. Engl. *47*, 5465–5469.

Walter, M.R., Windsor, W.T., Nagabhushan, T.L., Lundell, D.J., Lunn, C.A., Zauodny, P.J., and Narula, S.K. (1995). Crystal structure of a complex between interferon-gamma and its soluble high-affinity receptor. Nature *376*, 230–235.

Wedeking, T., Lochte, S., Birkholz, O., Wallenstein, A., Trahe, J., Klingauf, J., Piehler, J., and You, C. (2015). Spatiotemporally controlled reorganization of signaling complexes in the plasma membrane of living cells. Small *11*, 5912–5918.

Wilmes, S., Beutel, O., Li, Z., Francois-Newton, V., Richter, C.P., Janning, D., Kroll, C., Hanhart, P., Hotte, K., You, C., et al. (2015). Receptor dimerization dynamics as a regulatory valve for plasticity of type I interferon signaling. J. Cell Biol. *209*, 579–593.

Wilmes, S., Hafer, M., Vuorio, J., Tucker, J.A., Winkelmann, H., Lochte, S., Stanly, T.A., Pulgar Prieto, K.D., Poojari, C., Sharma, V., et al. (2020). Mechanism of homodimeric cytokine receptor activation and dysregulation by oncogenic mutations. Science *367*, 643–652.

Yang, N., Wang, X., Jiang, J., and Frank, S.J. (2007). Role of the growth hormone (GH) receptor transmembrane domain in receptor predimerization and GH-induced activation. Mol. Endocrinol. *21*, 1642–1655.

You, C., Richter, C.P., Lochte, S., Wilmes, S., and Piehler, J. (2014). Dynamic submicroscopic signaling zones revealed by pair correlation tracking and localization microscopy. Anal. Chem. *86*, 8593–8602.

Yu, J. (2016). Single-molecule studies in live cells. Annu. Rev. Phys. Chem. *67*, 565–585.

Zaks-Zilberman, M., Harrington, A.E., Ishino, T., and Chaiken, I.M. (2008). Interleukin-5 receptor subunit oligomerization and rearrangement revealed by fluorescence resonance energy transfer imaging. J. Biol. Chem. *283*, 13398–13406.

STAR★METHODS

KEY RESOURCES TABLE

REAGENT or RESOURCE	SOURCE	IDENTIFIER
Antibodies		
Monoclonal anti-MBP (R29.6)	Santa Cruz Biotechnology Inc.	Cat# sc-13564
Bacterial and virus strains		
E. coli Rosetta (DE3) pLysS cells	Novagen/Merck	Cat# 69451
Chemicals, peptides, and recombinant proteins		
DY-752 Maleimide	Dyomics	Cat# 752-02
DY-647P1 Maleimide	Dyomics	Cat# 647P1-03
ATTO 488 Maleimide	ATTO-TEC	Cat# AD 488-41
ATTO Rho11 Maleimide	ATTO-TEC	Cat# AD Rho11-41
ATTO 643 Maleimide	ATTO-TEC	Cat# AD 643-41
SNAP-Surface 647	New England Biolabs	Cat# XS9137 (discontinued on Sept 10, 2013)
Ampicillin	Biomol	Cat# 01503.25
IPTG	Thermo Fisher Scientific	Cat# R0392
HEPES buffer	PAN-Biotech	Cat# P05-01100
NaCl	Carl Roth	Cat# 3957.1
DNAseI	Sigma Aldrich/Merck	Cat# DN25
Lysozyme	Sigma Aldrich/Merck	Cat# L6876
Protease inhibitor	Serva	Cat# 39106
Imidazole	Carl Roth	Cat# 3899.4
DMSO	Carl Roth	Cat# A994.2
Cysteine	Sigma Aldrich/Merck	Cat# W-326305
Human IFNγ	Landar et al., 2000,	N/A
EDTA	Carl Roth	Cat# 8040.2
Guanidine hydrochloride	Sigma Aldrich/Merck	Cat# G3272
Ammonium acetate	Sigma Aldrich/Merck	Cat# A1542
Benzamidine	Sigma Aldrich/Merck	Cat# B-6506
(3-Glycidyloxypropyl)-trimethoxysilane	Sigma Aldrich/Merck	Cat# 440167
Acetone	Supelco/Merck	Cat# 100022
α, ω-Bis-amino-poly(ethylene) glycol (2000 g/mol)	Rapp Polymere	Cat# 112000-2
N,N-Diisopropylethylamine	Sigma Aldrich/Merck	Cat# 125806
N, N'-Diisopropylcarbodiimid	Sigma Aldrich/Merck	Cat# D125407
Trifluoroacetic acid	Sigma Aldrich/Merck	Cat# T6.220-0
Tris-NTA	Lata and Piehler, 2005	N/A
L-Alanyl-L-Glutamine	Biochrom	Cat# K0302
Accutase	Innovative Cell Technologies	Cat# AT104
Poly-L-lysine (PLL)-poly(ethylene) glycol (PEG)-RGD	You et al., 2014, Wedeking et al., 2015	N/A
PLL-PEG-Methoxy	You et al., 2014, Wedeking et al., 2015	N/A
Glucose	Carl Roth	Cat# 3774.1
Glucose Oxidase	Sigma Aldrich	Cat# 49180
Catalase	Sigma Aldrich	Cat# C-40
Methylviologen	Sigma Aldrich	Cat# 856177

(Continued on next page)

Continued

REAGENT or RESOURCE	SOURCE	IDENTIFIER
Ascorbic acid	Sigma Aldrich	Cat# A-4544
Deposited data		
Raw example data for testing SLIMfast	this manuscript	Zenodo: https://doi.org/10.5281/zenodo.5712332
Experimental models: Cell lines		
HeLa	DSMZ German Collection of Microorganisms and Cell Cultures GmbH	DSMZ No.: ACC 57
Recombinant DNA		
pET-21a	Novagen	N/A
pSems-26m	Covalys Biosciences	N/A
pSems-leader-mEGFPe-IFNAR1 (28–557)	this manuscript	N/A
pSems-leader-mEGFPm-IFNAR1 (28–557)	this manuscript	N/A
pSems-leader-SNAPf-mEGFPe-IFNAR1 (28–557)	this manuscript	N/A
pSems-leader-SNAPf-mEGFPm-IFNAR1 (28–557)	this manuscript	N/A
pSems-leader-SNAPf-mXFPm-IFNAR1 (28–557)	this manuscript	N/A
pSems-leader-mXFPm- IFNGR1 (18–489)	this manuscript	N/A
pSems-leader-mXFPe-IFNGR2 (30–337)	this manuscript	N/A
pet21a-aGFPnb-enhancer-cys-linker-YbbR-(PAS)5-H6	this manuscript	N/A
pet21a-aGFPnb-minimizer-cys-linker-YbbR-(PAS)5-H6	this manuscript	N/A
pSems leader-HA-mEGFP-MBP-(ALA)7KSSR	Wilmes et al., 2020	N/A
Software and algorithms		
CellSens Dimension	Olympus	RRID: SCR_014551
CorelDraw	Corel	RRID: SCR_014235
Matlab R2018a	MathWorks	RRID: SCR_001622
BIAevaluation 3.0	BIACORE	RRID: SCR_015936
OriginPro 9.0	OriginLab	RRID: SCR_014212
Software SLIMfast for single molecule analysis	this manuscript	Zenodo: https://doi.org/10.5281/zenodo.5712332
Other		
LB medium	Carl Roth	Cat# X968.3
Superdex 75 Increase 10/300 GL column	GE Healthcare/VWR	Cat# 75799-300
Anion exchange column HiTrapQ HP	GE Healthcare/Merck	Cat# GE29-0513
POROS HS 20 resin for IEC	ThermoFisher	Cat# 1332226
Superose 6 for SEC	GE Healthcare/Merck	Cat# GE29-0915
MEM	PAN-Biotech	Cat# P04-09500
Phenol red-free MEM	PAN-Biotech	Cat# P04-02500S1
FBS superior	Merck	Cat# S0615
Panexin NTA	PAN-Biotech	Cat# P04-95700
PBS	PAN-Biotech	Cat# P04-36500
MEM NEAA	PAN-Biotech	Cat# P08-32100
TetraSpec Microspheres, 0.2 μm, fluorescent blue/green/orange/red	ThermoFisher/Invitrogen	Cat# T7280
Round high precision glass cover slips, 24 mm	Carl Roth	Cat# PK26.2

RESOURCE AVAILABILITY

Lead contact

Further information and requests for resources and reagents should be directed to and will be fulfilled by the Lead Contact: Jacob Piehler (piehler@uos.de).

Materials availability

- Plasmids generated in this study are available via the lead contact upon request.

Data and code availability

- Raw example data for testing our software SLIMfast has been deposited at Zenodo and is publicly available (DOI is listed in the key resources table). All other original data reported in this paper will be shared by the lead contact upon request.
- The software SLIMfast for single molecule data analysis together with user instructions and an excel sheet containing all control parameters are also available at Zenodo (DOI is listed in the key resources table).
- Any additional information required to reanalyze the data reported in this paper is available from the lead contact upon request.

EXPERIMENTAL MODEL AND SUBJECT DETAILS

HeLa cells

HeLa cells were cultivated at 37 °C under 5% CO_2 in MEM with Earle's salts supplemented with 10% FBS superior (Merck KGaA), 2 mM L-Alanyl-L-Glutamine (Biochrom), 1% non-essential amino acids (Merck KGaA) and 10 mM HEPES buffer (Carl Roth). Cells were transfected with single or multiple plasmids at 30-40% confluency by calcium phosphate precipitation overnight, followed by medium exchange and regeneration for 2-3 days. The day before microscopy, cells were detached by room temperature treatment of Accutase (Innovative Cell Technologies) and seeded on microscopy cover slides coated with a 50/50 (w/w) mixture of poly-L-lysine graft copolymers of polyethylene glycol (PLL-PEG) that were modified with an RGD-peptide and a terminal methoxy group, respectively (Wedeking et al., 2015; You et al., 2014). Proof-of principle experiments of NB labeling were performed in phenol red-free MEM medium supplemented with FBS, while receptor dimerization experiments were performed in serum-free medium containing 10% (v/v) Panexin NTA (PAN Biotech).

METHOD DETAILS

Plasmids

Site-directed mutagenesis of wild-type (wt) mEGFP and mECFP, respectively, was carried out by PCR using a two-step protocol, which included the generation of two PCR fragments bearing the desired mutation using the T7 promotor and terminator sequences, followed by a second PCR using both mutated fragments as template. Resulting PCR fragments were then inserted into a custom pET-21a vector that lacked the C-terminal His-tag by the restriction enzymes *Eco*RI and *Age*I. The protein sequences of the final GFP variants mEGFPe and mECFPm can be found in Figure S1. The anti-GFP NBs enhancer (EN) and minimizer (MI) fused to a C-terminal hexahistidine tag were inserted into pET-21a. For fluorescence labeling, a C-terminal cysteine, followed by an ybbR-tag, a PAS repeat sequence and a terminal His$_6$-tag (amino acid sequence: GSCGSGSKLDSLEFIASKLAPASPASPASPASPASLEHHHHHH) was appended to the NB.

Vectors for expression of tagged receptors in mammalian cells were cloned using a modified version of pSems-26m (Covalys Biosciences) which includes the N-terminal leader sequence of Igκ followed by a hemagglutinin (HA)-tag (pSems-leader) under the control of a cytomegalovirus CMV promoter. Tags for labeling (GFP variants, SNAPf) were inserted into a multiple cloning site downstream of the HA-tag followed by the respective receptor lacking its N-terminal leader sequence. Specifications of expression vectors are detailed in the Table Features and applications of different receptor constructs.

Table. Features and applications of different receptor constructs

Denomination	Construct (residues)	Description and application
mEGFPe-IFNAR1	pSems-leader-mEGFPe-IFNAR1 (28-557)	mEGFPe-tagged IFNAR1 for quantifying labeling orthogonality
mECFPm-IFNAR1	pSems-leader-mEGFPm-IFNAR1 (28-557)	mEGFPm-tagged IFNAR1 for quantifying labeling orthogonality

(Continued on next page)

Continued

Denomination	Construct (residues)	Description and application
SNAPf-mEGFPe-IFNAR1	pSems-leader-SNAPf-mEGFPe-IFNAR1 (28-557)	DOL quantification by single molecule FRET
SNAPf-mEGFPm-IFNAR1	pSems-leader-SNAPf-mEGFPm-IFNAR1 (28-557)	DOL quantification by single molecule FRET
SNAPf-mXFPm-IFNAR1	pSems-leader-SNAPf-mXFPm-IFNAR1 (28-557)	DOL quantification by single molecule FRET
mXFPm-IFNGR1	pSems-leader-mXFPm- IFNGR1 (18-489)	mXFPm-tagged IFNGR1 for quantifying receptor dimerization
mXFPe-IFNGR2	pSems-leader-mXFPe-IFNGR2 (30-337)	mXFPe-tagged IFNGR2 for quantifying receptor dimerization

Expression and purification of NBs and GFP variants
Purification and fluorescence labeling of His6-tagged nanobodies
Competent *E.coli* Rosetta (DE3) pLysS cells (Novagen) were transformed with plasmids encoding for NBs. Cells were grown at 37 °C in LB medium supplemented with 100 μg mL^{-1} ampicillin until an OD_{600nm} of 0.6–0.8 was reached, when protein expression was induced by the addition of 0.8 mM IPTG followed by overnight culturing at 18 °C. Cells were pelleted by centrifugation, resuspended in HEPES-buffered saline (HBS – 20 mM HEPES pH 7.5, 150 mM NaCl) supplemented with DNAse, lysozyme and protease inhibitors and lysed by sonication. After ultracentrifugation (55.000 × g, 25 min, 4 °C, Type 70 Ti, Beckman Coulter), the supernatant was applied to an IMAC (5 mL HiTrap Chelating HP, GE Healthcare) by an FPLC system (ÄKTAprime, GE Healthcare). Proteins were eluted by a linear gradient with HBS buffer containing 500 mM imidazole. Collected NB-containing fractions were then fractionated by size exclusion chromatography (SEC) using a Superdex 75 Increase 10/300 GL column (GE Healthcare) in HBS buffer.

Site-specific fluorescence labeling of the NBs was conducted with a 2-fold excess of maleimide-fluorophore conjugates (diluted from 10 mM DMSO stocks) for 30 min at room temperature. The reaction was stopped by addition of a 3-fold excess of cysteine over the fluorophore and further incubation for 15 min, followed by SEC under the same conditions as described above. The degree of labeling (DOL) of all fluorophore-conjugated nanobodies was determined by UV/Vis spectroscopy using published (fluorescent dyes) or calculated (proteins) extinction coefficients and correction factors. Labeled and unlabeled nanobodies were flash-frozen in liquid nitrogen and stored at −80 °C until use.

Purification of mEGFP and mutants
Transformation and induction of protein expression in *E.coli* Rosetta (DE3) pLysS was carried out as described above. IPTG-induced cells were grown at 30 °C for 8 h and after a subsequent centrifugation, cells were resuspended in anion exchange chromatography (AEC) buffer A (20 mM HEPES pH 7.45, 10 mM NaCl) supplemented with DNAse, lysozyme and protease inhibitors. After cell lysis by sonication followed by ultracentrifugation, the supernatant was incubated at 60 - 70 °C in a water bath for 10 minutes in order to denature the majority of unwanted *E.coli* protein. Following another ultracentrifugation, the supernatant was subjected to an anion exchange column (5 mL HiTrapQ HP, GE Healtcare) equilibrated with AEC buffer A. GFP and GFP mutants were eluted under high salt concentrations in AEC buffer B (20 mM HEPES pH 7.45, 1.000 mM NaCl) and further purified by SEC as described above.

Expression, refolding, and purification of IFNγ and mIFNγ
Dimeric and monomeric IFNγ were expressed in *E. coli,* refolded, and purified, as previously described (Landar et al., 2000). Briefly, cells were grown in LB medium to an absorbance of 0.6 at 600 nm and then induced with 1 mM IPTG for 3 h. Inclusion bodies were isolated and solubilized in 8 M guanidine hydrochloride. Refolding was performed by rapid dilution into 10 mM ammonium acetate buffer (pH 7.0) containing 2.5 mM EDTA and 5 mM benzamidine. The proteins were purified by ion exchange chromatography (HS20 resin, ThermoFisher), followed by size exclusion chromatography (Superose 6, GE Healthcare).

Production and labeling of IFNγ cysteine mutant
IFNγ S66C was produced and purified as the wild-type. 45 μM of IFNγ S66C were mixed with 105 μM of maleimide functionalized DY-647P1 (Dyomics GmbH) to a final volume of 500 μL and incubated for 45 min in the absence of light at room temperature. Subsequently, the reaction was terminated by addition of L-cysteine (Sigma) at a final concentration of 300 μM and incubation for 15 min under the same condition. Unreacted dye was removed by size exclusion chromatography (Superdex 75 Increase 10/300 GL, GE Healthcare). The DOL of DY-647P1-labeled IFNγ S66C ($^{DY-647}$IFNγ) was estimated using absorption spectroscopy. The $^{DY-647}$IFNγ-containing aliquots were shock frozen in LN for long-term storage at −80 °C.

Simultaneous TIRF spectroscopy and reflectance interference detection
The interaction kinetics of purified NBs with different GFP variants was quantified by simultaneous real-time total internal reflection fluorescence spectroscopy and reflectance interference (TIRFS-RIF) detection in a flow-through system (Gavutis et al., 2005). In brief, the home-built setup employs white-light interference upon reflection at a 400 nm SiO_2 layer on a glass transducer for label-free detection of protein binding. Laser excitation via total internal reflection using a glass prism simultaneously

enables surface-sensitive fluorescence detection. mECFP and mEGFP were excited by a 405 nm or 488 nm laser, respectively, and fluorescence was filtered by bandpass filters between 465-500 nm for mECFP and 495-605 nm for mEGFP, before being detected by photomultipliers.

For immobilization of His-tagged proteins, TIRFS-RIF transducers were coated with a dense PEG polymer brush that was functionalized with tris-(nitrilotriacetic acid) (tris-NTA) as described in detail previously (Lata and Piehler, 2005). Oxygen plasma-treated transducer slides were first silanized with (3-glycidyloxypropyl)-trimethoxysilane at 75 °C for 50 min. After washing with dry acetone, the epoxy groups were reacted with molten pure α, ω-bis-amino-poly(ethylene) glycol with a molecular mass of 2.000 g/mol (Rapp Polymere) for 4 h at 75 °C. Unreacted PEG was removed by washing with water, followed by reacting the free amines with a the carboxyl group the tertiary butyl ester-protected multivalent chelator tris-NTA (10 mg mL^{-1} in chloroform) by N, N′-Diisopropylcarbodiimid (3.2 M) in presence of traces of N,N-diisopropylethylamine for 1 h at room temperature. The tertiary butyl ester-protected NTA groups of tris-NTA were in a last step deprotected by overnight incubation in pure trifluoroacetic acid.

Protein interactions were probed under flow-through conditions using HBS. NBs were immobilized by their His-tag on the Ni^{2+}-loaded tris-NTA surfaces to yield low densities of 0.1–0.2 ng mm^{-2} (fluorescent FPs) or ~1 ng mm^{-2} (fluorescent-dead FPs). mECFP and mEGFP mutants in varying concentrations were injected for 60 s under a constant flow rate of 4.2 μL s^{-1}, before the surface was rinsed for 6 min with HBS buffer with a flow rate of 10 μL s^{-1}. After each experiment, the surface was regenerated by washing with 500 mM imidazole in HBS. Kinetic and rate constants were extracted using the BIAevaluation 3.0 software (BIACORE) by applying a 1:1 Langmuir model.

Fluorescence spectroscopy

Fluorescence spectra were measured with the fluorimeter FP-6500 (Jasco) using Quarz Suprasil cuvettes (Hellma). Stock solutions of purified GFP variants were diluted with PBS (plus 1 mg/mL BSA) to a final concentration of 100 nM in 1 mL sample volume. 500 μL were taken from this sample and the corresponding purified nanobody was added to a final concentration of 200 nM. Excitation and emission peaks of the GFP variants were taken from www.fpbase.org (FPbase IDs: mEGFP: QKFJN; mECFP: MVN8T). Excitation spectra of GFP variants (EGFP, mEGFP and mEGFPe) and CFP variants (mECFP and mECFPm) were measured at $\lambda_{em} = 510$ nm and $\lambda_{em} = 475$ nm, respectively. Likewise, emission spectra of GFP variants and CFP variants were measured at $\lambda_{ex} = 488$ nm and $\lambda_{ex} = 433$ nm, respectively. Fluorescence spectra were normalized to the peak values of eGFP, mEGFP or mECFP in absence of NB and plotted using OriginPro 9.0 (OriginLab).

Fluorescence lifetime measurements

Fluorescence lifetime measurements were conducted on a confocal laser scanning microscope (FluoView 1000, Olympus, Japan) equipped with a FLIM/FCS upgrade kit (Picoquant, Germany) using a TCSPC module (PicoHarp 300) and a picosecond diode laser driver (Sepia II, PDL 828). For excitation of GFP variants, a picosecond pulsed 485 nm laser diode (LDH-D-C-485, Picoquant) at a repetition rate of 32 MHz was used. Excitation of CFP variants were performed with a 440 nm laser diode (LDH-P-C-440B) at 32 MHz repetition rate. Fluorescence was detected by a single photon avalanche detector (Picoquant) using a bandpass filter from 500-550 nm (BrightLine HC 525/50, Semrock) for GFP variants or from 465-500 nm (BrightLine HC 482/35) for CFP variants. All measurements were performed in a 50 μL droplet placed on a high-precision coverslip at room temperature (25°C). Fluorescence was collected with a 60x water immersion objective (UPLSAPO 60x, NA 1.2, Olympus) at 20 μm above coverslip inside the droplet in point scanning mode. Time-correlated single photon counting (TCSPC) histograms with a resolution of 8 ps were analyzed by the software SymPhoTime 64 (Version 2.5, Picoquant). All data was fitted by reconvolution fits within SymPhoTime using the data-derived instrument response function and a bi-exponential model. Only in the case of meGFPe+EN a single exponential model fit performed better. Final lifetime for each sample is given by the amplitude-weighted average lifetime.

Live-cell labeling

For testing labeling orthogonality, HeLa cell expressing either mEGFPe-IFNAR, mECFPm-IFNAR1 or variants thereof were simultaneously incubated with 10 nM of each [Rho11]EN and [DY647]MI for 5 min, followed by washing with PBS. During imaging, 2 nM of each [Rho11]EN and [DY647]MI were present in the medium.

For the determination of the effective degree of labeling (DOL) achieved in living cells, the respective GFP variant together with a SNAPf-tag were fused to the N-terminus of the transmembrane receptor IFNAR1 (SNAPf-meGFPe-IFNAR1, SNAPf-meCFPm-IFNAR1 and the corresponding mXFP variants thereof). HeLa cells expressing the respective constructs were in a first step labeled with 100 nM of SNAPsurface647 (New England Biolabs) in MEM medium at 37 °C for 15 min. After removal of unreacted dye by multiple washing steps with room temperature PBS, the cells were incubated with either 20 nM of [Rho11]EN or [Rho11]MI for 10 min. During imaging, 2 nM of the corresponding labeled NB was present in the medium.

Labeling of IFNGR1 and IFNGR2 N-terminally fused to mXFP variants was conducted by first incubating the cells with 3 nM EN for 5 min, followed by addition of 3 nM MI. For four-color experiments, equal concentrations (3 nM) of both EN and MI labeled with two different fluorophores (ATTO 488, ATTO Rho11, ATTO 643, Dy752) were applied in the same manner.

Single-molecule localization microscopy

Single-molecule imaging was carried out by total internal reflection fluorescence microscopy (TIRFM) using an inverted microscope (IX83-P2ZF, Olympus) equipped with a motorized quad-line TIR illumination condenser (cellTIRF-4-Line, Olympus). The dyes ATTO

488, ATTO Rho11, DY-647P1/ATTO 643 and DY-752 were excited using a 100× oil immersion objective (UPLAPO100XOHR, NA 1.5, Olympus) at 488 nm (LuxX 488-200, max. 200 mW, Omicron), 561 nm (2RU-VFL-P-500-560-B1R, MPB Communications), 642 nm (2RU-VFL-P-500-642-B1R, MPB Communications) and 730 nm (LuxX 730-50, max. 50 mW, Omicron), respectively. Fluorescence was filtered by a penta-band polychroic mirror (zt405/488/561/640/730rpc, Semrock) and excitation light was blocked by a penta-band bandpass emission filter (BrightLine HC 440/521/607/694/809, Semrock). Up to four channels could be simultaneously acquired by using the four quadrants of a single back-illuminated EMCCD camera (iXon Ultra 897, Andor Technologies) and a four-color image splitter (QuadView QV2, Photometrics). The latter is equipped with three dichroic beamsplitters at 565 nm, 630 nm and 735 nm (T565LPXR, 630 DCXR and 735DCXR, Chroma) and four single-band bandpass emission filters (BrightLine HC 520/35, BrightLine HC 809/81, Semrock; ET 600/50, ET 685/50, Chroma). For dual channel imaging, only the orange (ATTO Rho11) and red (Dy647-P1/ATTO 643) channel were acquired. To obtain a pixel size of 100 nm, an additional 1.6x magnification was introduced (IX3-CAS, Olympus). The focus was continuously stabilized during the experiment by a hardware autofocus-system (IX3-ZDC2, Olympus) using an internal laser diode at 830 nm.

Four-color experiments required a fast in-frame alternate excitation scheme, since simultaneous excitation of ATTO488 and cyanine dyes (DY647P1/ATTO643, DY-752) resulted in high photo-bleaching rates of the far-red dyes (Figure S5B). We therefore established a camera-based alternate triggering mode using two function generators directly linked to the laser sources for ultra-fast on/off switching. Here, the rising edge of the camera exposure signal (TTL signal from camera) serves as the master trigger for the first function generator (HMF2525, Hameg) to pulse the 561 nm, 642 nm and 730 nm laser lines simultaneously. We typically use a burst of 15 short pulses (1 ms high (laser on)/1 ms low (laser off)) within a single 33 ms long frame. The falling edge of these pulses are triggering a second function generator (AFG-2225, GW Instek) pulsing the 488 nm laser with the same high/low signal. The trigger signals for the 488 nm and the 730 nm laser are directly linked to the electronic shutter of the laser heads shutting down the laser output in less than 2 μs. The 560 nm and the 642 nm laser are switched within < 1μs via an acousto-optical tunable filter (TF525-250-6-3-GH18A, Gooch & Housego) linked to an eight channel digital frequency synthesizer (MSD040-150-0.2ADM-A5H-8X1, Gooch & Housego).

In all imaging experiments, an oxygen-scavenging system composed of glucose oxidase (4.5 U·mL^{-1}), catalase (540 U·mL^{-1}) and glucose (4.5 mg mL^{-1}) was added to increase photostability. Additionally, a photoprotectant redox system composed of ascorbic acid and methyl viologen (both 1 mM) was applied (Vogelsang et al., 2008). For each channel, penetration depth of the evanescent field as well as laser excitation intensities (typically 50-500 W/cm^2) were optimized to obtain comparable signal to background levels in each channel (Figures S5C and S5D). Viable cells showing typical surface densities of 0.1–0.8 copies/μm^2 (Figures S5C and S5D) were imaged at 30 frames per second for typically 150 consecutive frames using CellSens 2.2 (Olympus) as acquisition software. For quantifying the DOL by smFRET, frame-by-frame alternating excitation at 642 nm and 560 nm lasers was employed in combination with dual-color image acquisition of donor and acceptor fluorescence by using the image splitter and filters mentioned above.

QUANTIFICATION AND STATISTICAL ANALYSIS

Single molecule data evaluation

Dual- and quad-color raw images were evaluated using an in-house developed Software for Localization-based Imaging in Matlab (SLIMfast). SLIMfast was used to capture individual protein-protein interaction events by single molecule (co-)localization and (co-)tracking as well as analyze their diffusion behavior.

For channel registration, 200 nm TetraSpeck beads (Thermo Fisher Scientific) as multi-color fiducials visible in all fluorescence channels were used. While the TetraSpeck beads are not labeled with NIR dyes, the high brightness of the far-red channel can be used to obtain a reasonable crosstalk in the NIR-channel upon excitation at 642 nm. After bead localization in all spectral channels, we calculated projective transformation matrices to spatially align up to four channels with sub-pixel accuracy correcting for relative translation-, rotation- and scaling factors with respect to the defined reference channel.

Localization of individual fluorescence emitters against noise was done at a set error probability of 10^{-5} (less than 1 false positive detection per frame) with an apparent point spread function estimated robustly from each respective channel using the multi-target tracking algorithm (Serge et al., 2008). Immobile emitters were identified by spatiotemporal cluster analysis using a modified density-based spatial clustering of applications with noise algorithm DBSCAN (Niewidok et al., 2018; Sander et al., 1998). Briefly, emitters are scored as immobile particles if there exists a significant accumulation of localizations within a spatial (here derived from the localization precision (Rieger and Stallinga, 2014)) and temporal window (iteratively decreasing to a set minimum of 5 frames). Background nanobody binding to the coverslip surface and endocytosed receptors may significantly contribute to the immobile fraction. In this work, we therefore excluded immobile molecules from further tracking, co-tracking and PICCS analyses, which is optionally provided within the SLIMfast software. Single molecule tracking was carried out using the algorithm utrack (Jaqaman et al., 2008). Upper boundaries for particle linking were established upon a prior robust evaluation of the frame-to-frame nearest-neighbor distribution. Gap closing with a maximum of 5 frames were allowed to account for missing localizations due to e.g. fluorescence blinking. Trajectories with an observation time ≥10 frames (≥320 ms) were used for further processing.

In order to detect complex formation we performed co-tracking analysis between spectral channels. Particles classified as immobile (s. above) were removed for this analysis if not stated otherwise because the analysis was more robust under these conditions (cf. Figure S2F). Frame-by-frame co-localization within a set radius of typically 150 nm (cf. Figure S2D) followed by tracking

of co-localized emitters applying utrack with the same parameters as described above. Molecules co-diffusing for ≥ 10 frames (≥ 320 ms) were identified as interaction events. Relative heterodimerization levels were determined based on the fraction of co-localized particles which were previously assigned to mobile trajectories. Moreover, heterodimerization levels were related to the least expressed receptor subunit as this subunit limits the absolute number of co-localization events:

$$\text{Relative co} - \text{tracking} = \frac{AB}{A} \text{ with } A < B. \qquad \text{(Equation 1)}$$

Here, A, B and AB are the total number of localizations observed for each individual receptor channel and the co-localized receptor subunits, respectively. Relative homodimerization levels were corrected for dimers stochastically double-labeled with the same fluorophore species:

$$AB^* = \frac{AB}{2 \times \left[\left(\frac{A}{A+B} \right) \times \left(\frac{B}{A+B} \right) \right]}, \qquad \text{(Equation 2)}$$

$$\text{relative co} - \text{tracking} = \frac{2 \times AB^*}{(A+B)}, \qquad \text{(Equation 3)}$$

where AB* represents the corrected total number of co-localized receptor subunits (total number of dimers).

Particle image cross-correlation spectroscopy (PICCS)

To quantify receptor interaction we performed particle image cross-correlation spectroscopy (PICCS) (Semrau et al., 2011). For comparison with the co-tracking data, immobile particles were also removed prior to PICCS analysis. The cumulative cross-correlation function between respective channels was sampled logarithmically from the localization data up to a maximum length of 1 µm. To avoid border effects, the source channels' cell mask was first eroded given the set maximal cross-correlation. For each channel pair the cumulative cross-correlation was fitted according to:

$$C_{cum}(r) = \alpha \left(1 - e^{-\frac{r^2}{2\sigma^2}} \right) + \rho \pi r^2 \qquad \text{(Equation 4)}$$

with α quantifying the degree of complex formation in the source channel with estimated correlation length σ and ρ being the receptor density in the correlated channel. The fits are conducted in a running window of 2 frames with constraints set on the correlation length (here 20-120 nm for the positive control covering the potential range due to finite localization precision and fixed correlation length in case of the negative control) and respective channel densities determined previously. Finally, we calculated robust parameter averages over time allowing up to 50% outliers via univariate minimum covariance determinant analysis (Rousseeuw and Leroy, 1987; Verboven and Hubert, 2005). The values reported for the correlated fractions in Figure S5 (2-color experiment) are with respect to the less labelled source channel and in Figure S9 (4-color experiment) the correlated fractions are summed over the two correlated channels labeled in different colors.

Degree of labeling (DOL)

The effective nanobody DOL was determined by the number of localized molecules in the nanobody donor [nb] and acceptor [$FRET$] channel with donor excitation and the acceptor channel with acceptor excitation [$fSNAP$]. In order to account for false-positive background localizations, untransfected HeLa cells were subjected to the exact same labeling procedure, image acquisition and data analysis ($bg[FRET]$ and $bg[nb]$):

$$DOL_{nb} = \frac{[FRET] - bg[FRET]}{[fSNAP] - bg[fSNAP]}, \qquad \text{(Equation 5)}$$

$$DOL_{fSNAP} = \frac{[FRET] - bg[FRET]}{[nb] - bg[nb]} \qquad \text{(Equation 6)}$$

Mean squared displacement analysis

Diffusion properties were extracted from pooled single trajectory mean squared displacement (MSD) analysis for all trajectories with a lifetime greater than 10 frames. Here, MSD plots from different channels correspond to different receptor subunits. MSD plots of receptor complexes were collected from co-trajectories of both channels. The instantaneous diffusion coefficient (first 10 data points; $\tau_{max} = 330$ ms) was estimated for each cell. Therefore, we calculated MSD-time curves for observed trajectories and performed weighted (by the inverse expected error) fits according to the model for Brownian diffusion (Michalet, 2010):

$$MSD(\tau) = 4D \cdot \tau - \frac{4}{3}Dt_e + 4 \cdot \sigma^2. \qquad \text{(Equation 7)}$$

Here, τ is the lag time, D the diffusion coefficient, t_e the exposure time, and σ the localization precision. Local estimates of the diffusion coefficient showing an excessive standard error on the estimates were discarded. Finally, the cell-wide global average was extracted robustly from the Gaussian distribution of log-transformed diffusion coefficients using the minimum covariance determinant method (Rousseeuw and Leroy, 1987).

Single molecule FRET analysis

For single-molecule FRET analysis, representative trajectories of co-localized receptors were chosen. Donor and acceptor intensities were determined from the fitted 2D Gaussian profile along each trajectory. The FRET efficiency E was calculated from the mean donor intensity 500 ms before (I_{DA}) and 500 ms after (I_D) photobleaching of the acceptor

$$E = 1 - \frac{I_{DA}}{I_D}. \qquad \text{(Equation 8)}$$

The respective donor-acceptor distance was calculated from the FRET efficiency E according to the Förster equation:

$$r = \sqrt{(1-E)/E} \cdot R_0. \qquad \text{(Equation 9)}$$

parameterizing the Förster radius R_0 = 6.9 nm for Rho11/AT643 as provided by the manufacturer (ATTO-TEC GmbH).

Statistical analysis

Box plots were used for visualization and indicate the data distribution of 2nd and 3rd quartile (box), median (line), mean (square) and 1.5× interquartile range (whiskers). Each data point represents the analysis from one cell with a minimum of 10 cells measured for each condition. Statistical significances were determined performing an unpaired student's t test. Asterisks represent following *p-value*s: ns - $p > 0.05$; * - $p \leq 0.05$; ** - $p \leq 0.01$; *** - $p \leq 0.001$.